ROTORDYNAMIC PERFORMANCE OF A ROTOR SUPPORTED BY THREE PAD HYBRID AIR FOIL BEARING WITH CONTROLLED AIR INJECTION

by

SANDESH GUDEMANE

Presented to the Faculty of the Graduate School of

The University of Texas at Arlington in Partial Fulfillment

of the Requirements

for the Degree of

MASTER OF SCIENCE IN MECHANICAL ENGINEERING

THE UNIVERSITY OF TEXAS AT ARLINGTON

MAY 2013

Acknowledgements

I would like to express my deep appreciation to my committee chair, Dr. Daejong Kim, without his guidance and support this thesis would not have been possible. I am also grateful to Dr. Seiichi Nomura and Dr. B. P. Wang for serving as my committee members.

I want to express my gratitude to Kermit Beird and the machinists from machine shop for helping me at each stage in the modification of bearing components. I also want to thank my colleagues and friends at Microturbomachinery and Energy Systems Lab for their help and support.

And last but not the least, I would thank my family for constant encouragement and the confidence they showed in my abilities for all these years. This thesis is a result of their sacrifices for me and, definitely God's grace.

May 3, 2013

Abstract

ROTORDYNAMIC PERFORMANCE OF A ROTOR SUPPORTED ON A THREE PAD HYBRID AIR FOIL BEARING (HAFB) WITH CONTROLLED AIR INJECTION

Sandesh Gudemane, MS
The University of Texas at Arlington, 2013

Supervising Professor: Dr. Daejong Kim

Air Foil Bearings have found their place in the commercial applications of turbo machinery. They are cleaner and more reliable at high speeds than their conventional counterparts (Rolling Element Bearings). Low drag friction and apparently no contact during the operation results in a better service life and superior rotor-dynamic performance of the air foil bearings (AFBs). With these advantages AFB has proved to be a suitable option for oil-free turbo-machinery. Further development in AFBs suggest that pressurizing these bearings externally results in remarkably better load carrying capacity, heat dissipation and a more stable rotor. These externally air pressurized bearings which operate under hydrodynamic pressure with a hydrostatic lift are called Hybrid Air foil Bearing (HAFB).

One of the major rotordynamic problem encountered in high speed turbomachinery is the subsynchronous vibration. If left unchecked, the higher amplitudes of subsynchronous vibrations can cause some serious damage to the bearing as well as the turbomachine. A previous study by Kim, D and Varrey, M [1] on a rotor of 4.84 kg supported by a three pad HAFB demonstrated the effects of increased air feed on the subsynchronous vibrations. The tests suggested an increase in the onset speed of

subsynchronous vibration with higher pressures but minimal changes were observed in the natural frequencies.

The present work is to numerically investigate the feasibility of controlled air injection to stabilize the rotor at high speeds. The intention is to push the rotor to higher eccentricity by loading it in one direction with the help of controlled air injection. The numerical analysis is carried out by orbit simulation method on a three pad HAFB of diameter 49 mm to test the whirl instability. The orbit simulation result suggests a delay in the appearance of subsynchronous vibrations. Further, experiments are carried out on a similar arrangement with the same rotor-bearing parameters. The shaft is loaded at the witness of subsynchronous vibrations (instability) to validate the simulation results. In actual practice out of the three air injection lines, one of the air injection lines is blocked to allow shaft loading and to notice its effects on the subsynchronous vibrations. The results were favorable, the amplitudes of subsynchronous vibrations diminished instantly suggesting a stable rotor as expected.

Table of Contents

List of Illustrations

List of Tables

Nomenclature

x, y, z	Fluid flow Cartesian coordinate defined with x along bearing circumferential direction, y across film thickness, and z along bearing axial direction
u, v, w	Air flow speed within the film
t	Time measured in second
p	Absolute pressure within fluid film
P	Non-dimensionalized pressure
C	Nominal bearing clearance in [m]
h	Local fluid film thickness in [m]
H	Non-dimensionalized film thickness
d	Air foil bearing damping coefficient with first subscript representing direction in cartesian coordinate and second subscript representing bearing response
k	Air foil bearing stiffness coefficient with first subscript representing direction in cartesian coordinate and second subscript representing bearing response
D	Non-dimensionalized damping coefficient with first subscript representing direction in cartesian coordinate and second subscript representing bearing response
K	Non-dimensionalized stiffness coefficient with first subscript representing direction in cartesian coordinate and second subscript representing
P_a	Atmospheric pressure [N / m^2]

R	Bearing Radius [m]
r_p	Preload
τ	Non-dimensionalized time
ω	Rotor speed [rad / s]
ω_s	Excitation frequency [rad / s]
μ	Air dynamic viscosity [$N \cdot s / m^2$]
A_o	Effective bump area covered by a single bump [m^2]
W_o	Reference Load [N]
ν	Frequency ration ω_s / ω
η	Structural damping loss factor

Chapter 1

Introduction

The ever demanding high speed and clean bearing use in turbo machinery is the reason for extensive research in the air foil bearings. The notion of air foil bearings dates back to 1960s when the first generation foil bearings were developed. In the recent years the air foil bearings have found many applications. They are typically popular in Turbo-compressors, Air Cycle Machines (ACMs), Turbochargers, Micro-gas Turbines (MGTs) and other Micro-turbomachinery due to the fact that they are lighter, cleaner and offer more compact work environment. In air foil bearings, air acts as the lubricating medium between the rotor and the bearing hence negating the need for oil. The other major advantage is the wide operation range from temperatures over $500^{o}C$ to cryogenic temperatures where the oil film ceases to operate.

The first air foil bearing was designed in 1969 for the Air Cycle Machine of DC-10's, they proved to be more reliable and lighter than the previously used ball bearings [2]. With further success of air foil bearings in Air Cycle Machines (ACMs) of Boeing 747 which demonstrated a Mean Time between Failure (MTBF) of 100000 hours almost all airplanes by the year 1988 including, F-16s, F-18s and Boeing 777 had the air foil bearings installed in their ACMs.

1.1 Air Foil Journal Bearing

A generic air foil bearing (AFB) comprises of a smooth top foil, compliant support structure and the bearing sleeve. There are three successful air foil bearing designs a) Bump-type Air Foil Bearing, b) Metal-Mesh type Air foil Bearing and c) Leaf-Type Air Foil Bearing as shown in Figure 1-1. For the present study, a Bump-type Air Foil Bearing is used. A circular single pad bump-type air foil bearing with a continuous top and bump foil is shown below in Figure 1-1 (A). When the shaft is at rest, it is in direct contact with the

top foil and the corrugated bump foil supports the top foil. There always exist an offset between journal and the bearing center termed as the eccentricity, which decides the hydrodynamic pressure that will be generated in the bearing during operation. In Figure 1-1 (A), the top foil and the bump foil are welded to the bearing sleeve at the same spot to avoid its displacement during operation. During operation, the journal rotates from the free end (leading edge) to the fixed end (trailing edge) to avoid inter-locking. The AFB show superior dynamic performance during operation with improved mechanical efficiency due to better damping as compared to the rolling element bearings. The compliant bump foil provides the bearing structural stiffness and the relative motion between top and bump foil as well as the bump foil and bearing housing provide coulomb type damping. For better results, these foils are made up of specific chromium-nickel alloy called Inconel. The most widely used grades of Inconel for making bump foils are Inconel-718 and InconelX-750, which show amazing springback properties.

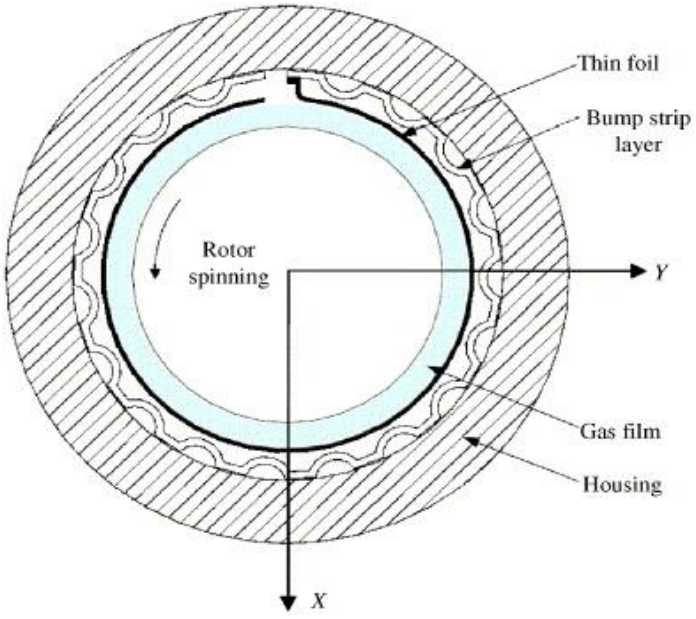

(A)

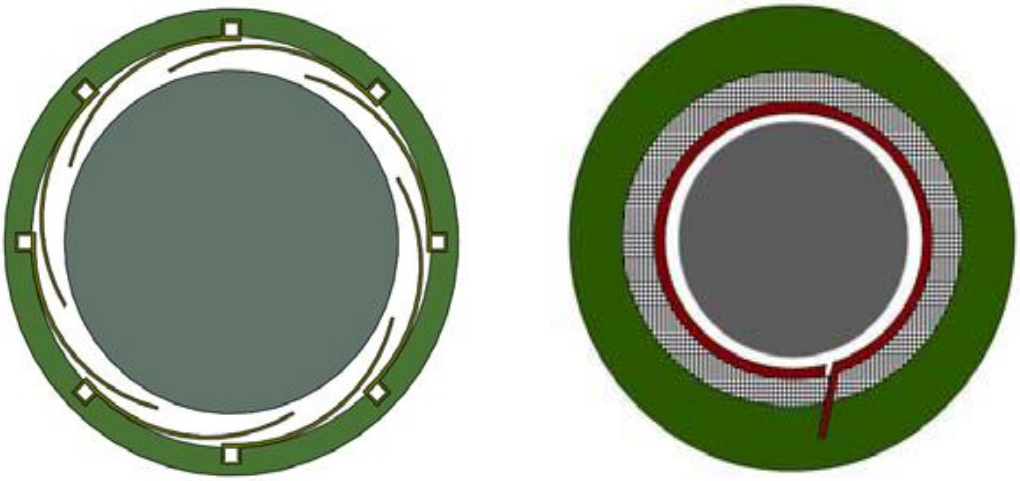

(B) (C)

Figure 1-1 Air Foil Bearings (A) Bump-Type Air Foil Bearing (B) Leaf-Type Air foil Bearing (C) Mesh-Type Air Foil Bearing[3]

1.1.1 Principle of Operation:

The rotor supported in Air Foil Bearings (AFBs) follow two major mechanisms for its operation. (a) Wedge Effect, the rotor and the bearing surface is separated by a small gap called the clearance. Now, when the rotor starts spinning a converging wedge is formed between the journal and the bearing. A positive air pressure builds between the two converging surfaces due to this wedge. The air pressure developed keeps the rotor air borne. However in practical cases, there exists air leakage from the sides and hence the wedge effect is relatively small. The other phenomenon noticed is the (b) Squeeze film effect, when the gas in the bearing clearance is squeezed suddenly, the escaping gas molecules feel some resistance from the surrounding molecules and a positive pressure gradient is developed just like in the wedge film effect.

The greater service life in AFBs is attributed to the frictionless operation between the rotor and the bearing but in AFBs a lot of dry rubbing is also noticed during start and stop of the shaft. To reduce this friction the top foil is coated with solid lubricants with low

coefficient of friction like the Teflon (In present study Bearing Design I was Teflon coated while Bearing Design II was not). Other than the wear, frequent start/stop friction brings up an issue of heat. This heat adds up to the overall operational heat generated in the bearing. If the bearing operation requires frequent start/stop the heat generated can be substantial. The heat dissipation in AFBs is a prime concern and need to be dealt with, the hydrodynamic pressure developed between rotor and bearing is good to keep journal air borne but it does little for heat dissipation.

1.2 Introduction to Hybrid Air Foil Bearing

The Hydrodynamic air foil bearings are well suited for mid size turbomachinery applications. They operate pretty well for rigid journal rotors of diameter less than 4 inches. However, with increase in rotor size, foil bearing load capacity does not match up with the increase of rotor weight due to scaling laws, the rotor weight can be assumed to grow third power with size whereas the load capacity of the AFB follows a square function. For high-speed turbomachinery applications a bearing operates with DN (where D=diameter and N=speed of rotor) number of 3-5 millions. A large AFB (150 mm in diameter) was tested at 1200^{o} F [4], the bearing operated for about eight minutes before sudden rise in temperature followed by severe rubbing marks were observed. Foil bearings of such large magnitudes pose thermal challenges and bump foil compliance under high loads.

The concept of Hybrid Air Foil Bearing (HAFB) was devised by Kim and Park [5] to overcome the cooling and the load capacity problems. A rotor in a hybrid air foil bearing operates in hydrodynamic pressure under hydrostatic pressure lift. HAFB was chiefly designed to overcome start/stop friction in the rotor-bearing system. An orifice is attached to the top foil of the bearing which feeds the air directly on to the shaft. The air feed rate affects rotor stability and the dynamic behavior of HAFB. It also affects the

stiffness and the damping characteristics of the bearing. Increasing air feed pressure suggests a decrease in both direct and cross-coupled stiffness while the damping shows an increasing trend [6].

The general single pad (pad is a combination of top foil and bump foil) bearing fail to take loads in all directions, they also reflect instability issues at high speeds. Hence, multi-pad bearings are used for the present research. In the present research, a three-pad bearing as shown in Figure 1-2 is used with each pad spacing at 120 ^{o}. The initial bearing design (Bearing Design I) had three top foils and six bump foils. Two bump foils supporting each top foil. The distance between the bearing center and top foil center is called the hydrodynamic offset of the bearing. This configuration is specifically good to create a non-uniform clearance and allow some amount of offset preload. The offset preload is essential to avoid instabilities at high speeds [7].

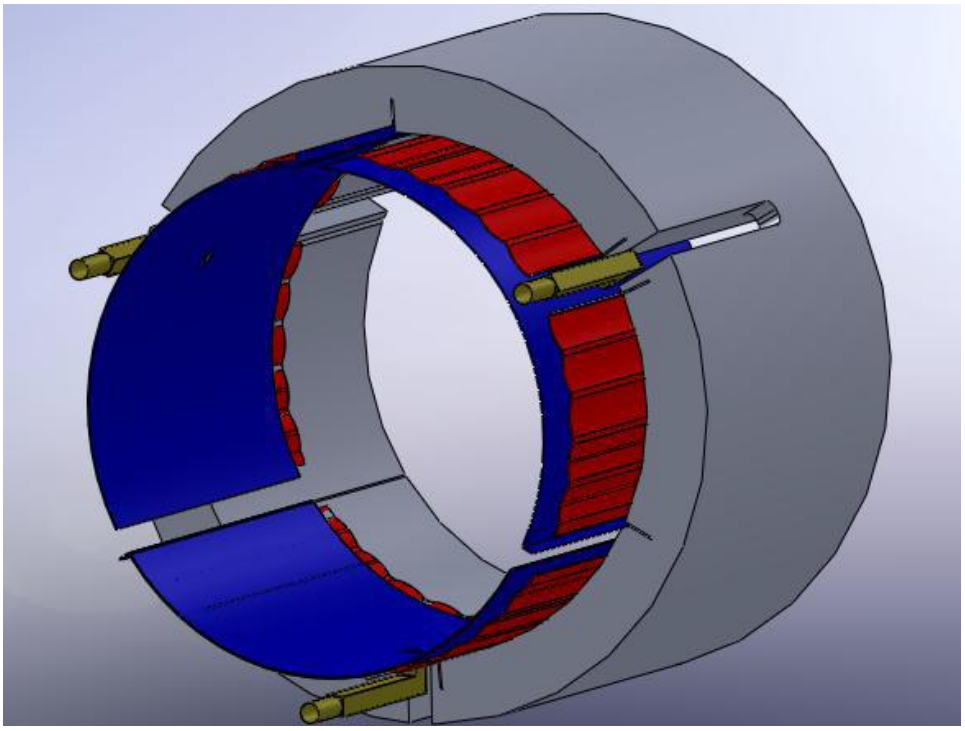

Figure 1-2 Solid Model of a Hybrid Air Foil Journal Bearing

1.3 Introduction to Air Foil Thrust Bearing

The Air Foil Thrust Bearing has a similar design and working principle as that of the journal AFB, they have a compliant bump foil which sits beneath a set of smooth top foils. Each combination of bump foil and the top foil is called a pad. An Air Foil Thrust Bearing (AFTB) can have several discrete pads and these pads are spot welded to the thrust plate to avoid displacement during bearing operation. Just like in the radial AFB, the Air Foil Thrust Bearing (AFTB) works on the wedge phenomenon. During operation, the wedge in AFTB accounts from the deflections in the pad caused due to axial load from the thrust disc. The converging wedge gap (Figure 1-3) develops the necessary pressure for bearing operation. The only difference here is the direction of the rotation, which is opposite to that of the Journal AFB.

The thrust load from any small turbocompressors or engines is large as compared to its size. To support large loads from turbocompressor or turboengines, a bigger (in diameter) thrust bearing is desired. However, larger diameter thrust bearings may result in DN (D is diameter in mm and N is speed in RPM) above 8 million DN as compared to 3-5 million DN in radial AFBs which is very difficult to achieve due to stability issues [8].

The studies and research on AFTB are very few as compared to Journal AFBs. However, an AFTB with novel features and design is used for current research. The thrust bearing used for current research was recently developed at Microturbomachinery and Energy Systems Laboratory at University of Texas at Arlington and has major features of the AFTB developed by Lee and Kim [8]. The thermal management and the manufacturability of AFTB has always been an important concern but the newly developed thrust bearings surmounted both issues. The cooling occurs radially in these bearings and the manufacturing capability is discussed later in Chapter 3.

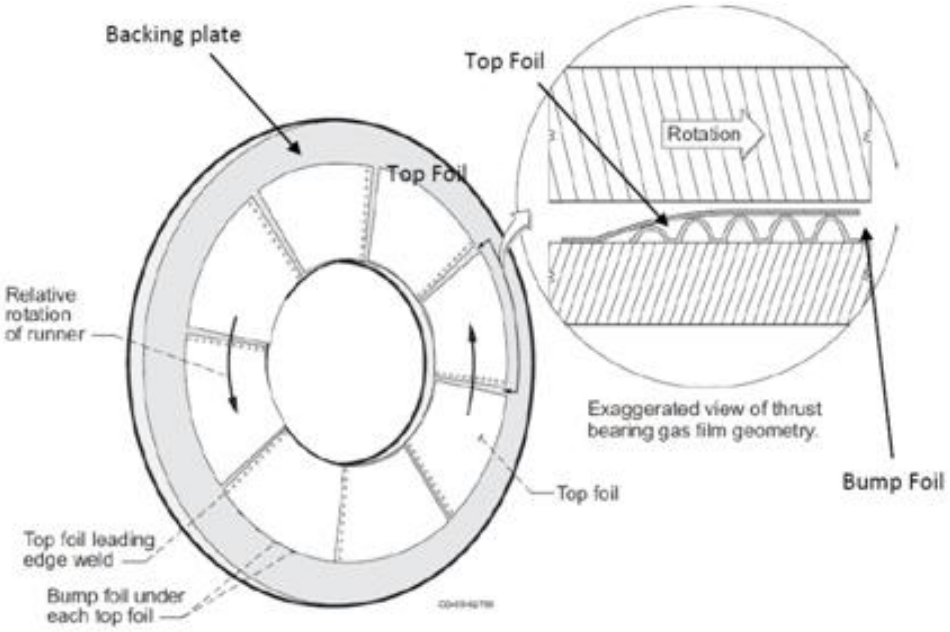

Figure 1-3 Air Foil Thrust Bearing [9]

1.4 Literature Review

One of the major problems encountered in the hydrodynamic bearings is the heat generation and load capacity. HAFB with external air pressure supply is the solution for both. Earlier, axial air supply for cooling was a common approach as used by San Andreas and Rubio [10]. They used a hollow stainless steel shaft supported at two ends. The two bearing consists of five bump foils and a Teflon coated top foil. Air was forced into the bearing axially ranging from 40kPa to 340kPa. The supply pressure did not affect the hydrodynamic operation of the bearings. However, the increase in pressure resulted in the reduction of amplitude of synchronous motion at critical speeds. In addition, a decrease in the subsynchronous motions was observed, with further increase of pressure the subsynchronous frequency splits into two other frequencies. Rubio [10] suggested the

decrease in the subsynchronous amplitudes was due to the reduction in the net circumferential flow (and hence cross-coupled stiffness) within the bearing due to external air feed. Though the bearing performed well for numerous tests it showed signs of severe rubbing and coating wear.

Kim and Park [5] used a flexible steel tube orifice to pressurize a multiple compression spring bearing. The intention was to lift off rotor before it starts to rotate and hence diminish the wear. Orbit simulations predicted higher critical speeds and higher load capacities than their hydrodynamic counterpart. Kumar and Kim [6] extended the idea of HAFB to compliant bump foil bearing. Moreover, with its computational model (Linear Perturbation Method) they predicted stiffness and damping of the Hybrid Air Foil Bearing. They demonstrated, with increase in supply pressure the rotor tries to center itself and there is a decrease in direct as well as cross-coupled stiffness whereas, an increase was observed in damping. The importance of supply pressure was obviously not restricted to cooling alone but also the rotor-bearing characteristics.

San Andreas and Wilde [11] performed a series of tests on a three lobed, pre loaded gas bearing. Each bearings housing is sealed with o-ring to pressurize the housing section. Higher feed pressure seemed to increase the bearing stiffness and critical speeds including the threshold speeds of instability with a decrease in cross-coupled stiffness hence suggesting a more stable rotor. Wilde and San Andreas [12] further performed the tests and compared it with linear rotor-dynamic analysis (bearing modeled using a FE program to solve Reynolds equation). Though it showed some discrepancy, the increase in air feed showed decrease in damping ratio and higher threshold rotor speeds as expected. It is interesting to note the ratio of cross-coupled stiffness to damping force remained constant to 0.50 irrespective of the feed pressure. A proper modeling and further tests are to be done to eliminate the discrepancy.

Later, Zhu and San Andreas [13] did a study on the rotor stability of a rotor supported on the flexure pivot tilting pad gas bearings (FPTPBs). The FPTPB are superior in performance to the three lobed gas bearings. With the increase in external air feed the bearing showed similar results. It showed an increase in direct stiffness and drop in the whirl frequency ratio. The interesting phenomena observed here was the rapid increase in load with the increase in feed pressure. A similar principle is followed for the current tests. The idea is to load the rotor by increasing the air feed rate and hence comment on its stability.

Recently, Varrey and kim [1] tested a HAFB with added imbalance masses and different air feed rate. The motor was set at a constant speed of 28000 rpm and the pressure was increased from 2.67 to 4 bar the subsynchronous amplitude decreased from 40 microns to 3 microns and the sub synchronous frequency increased slightly. A similar phenomenon is observed for in phase imbalance. Not much difference was seen at critical speeds and not much can be said about the stiffness, damping and natural frequency around the critical speeds. However, the cross-coupled stiffness decreased at excitation frequency. There was also a decrease in synchronous damping but the difference is minute, also the change in natural frequency was negligible.

1.5 Objective of current research

The load and the eccentricity play a major role in the bearing stability other than the bearing design and the configuration. From the previous mentioned studies, we can conclude that the air feed has some superior effect on rotor stability and on the load capacity of the bearing. The present study is to numerically establish the beneficial effects of controlled air injection on the rotor stability. Theoretically, for fluid bearings a shaft with greater eccentricity tends to greater stability. In order to increase shaft eccentricity the shaft is often loaded in one direction. The present simulations create an

external load on the shaft by blocking bottom air supply to the bearing and maintaining flow from the top two air lines. These non-linear orbit simulations suggest whirl instability (onset of subsynchronous vibrations) for different conditions. The simulation solves the Reynolds equation simultaneously with the journal and bump dynamic equations at each time step. Hence, it gives a close approximation of whirl instability for both the cases [all air feed lines open and bottom air feed line blocked].

Further, test runs are conducted on a similar three-pad HAFB to experimentally validate the effects of controlled air injection. The intention is to block the bottom air injection line of both (front and rear) bearing at subsynchronous vibrations and record rotor behavior. The initial few test runs were flawed due to rotor damage well before the appearance of sub-synchronous vibrations (discussed in Appendix B Shaft Failure). Hence, consecutive test runs were conducted at preliminary stage of subsynchronous vibrations. The tests results were recorded for a range of speeds and at different pressures to corroborate the results from orbit simulations.

Chapter 2

Methodology

The high energy densities and flow rates as required in modern turbo-machinery can only be achieved with high rotor speeds. However, with high rotor speeds are associated rotor stability problems namely shaft whirl, vibrations and other instabilities. These issues are factors of bearing-rotor system together and need to be dealt carefully. Every shaft has some amount of imbalance, which accounts for whirling. Moreover, when this whirling frequency is synchronous to the shaft speed it is termed as synchronous vibration. In most cases, synchronous vibration is not dangerous unless the imbalance is high. The more severe rotordynamic problem is the subsynchronous whirl, which appears when the whirl frequency falls below the shaft speed frequency. Most instability can be reduced by carefully designing the rotor with reduced imbalance and addition of correction masses but the subsynchronous vibrations are least susceptible to rotor imbalance. Kim and Varrey, [1] demonstrated the onset speed and the frequency of subsynchronous vibration was nearly the same for added imbalances except for slight rise in their amplitude. Subsynchronous vibrations are self excited, mostly promoted by the cross-coupled stiffness or internal friction. The approach for a stable rotor lies in either significantly reducing the amplitudes of subsynchronous vibrations or delaying their onset. Once the rotor-bearing system is designed, a possible way of achieving rotor stability in HAFB is by controlling air injection to increase rotor eccentricity.

2.1 Theory

The relationship between eccentricity and whirl frequency ratio was long established for circular fluid film bearings and the same relationship can be extended to preloaded offset bearings. Figure 2-1 [taken from [14]] shows the whirl frequency ratio (WFR), drop for higher values of eccentricity. The whirl frequency (ratio of self-sustaining

frequency to threshold frequency of the rotor) is inversely proportional to the rotor stability and hence Figure 2-1 implies a more stable rotor for higher values of eccentricity ratios. Similarly, Figure 2-2 shows a rise in threshold rotor mass for stability with eccentricity. Both plots indicate a very stable shaft operation for eccentricity ratios around 0.75 or higher.

The whirl frequency ratio and the dimensionless threshold rotor mass are related in the following way,

$$p_{Th}^{\ 2} = \frac{K_{eq}}{\nu^2} \tag{2-1}$$

Where, $\nu^2 = \left(\frac{\omega_S}{\omega_{Th}}\right)^2 = \frac{\left(K_{eq} - K_{XX}\right)\left(K_{eq} - K_{YY}\right) - K_{XY}K_{YX}}{D_{XX}D_{YY} - D_{YX}D_{XY}}$

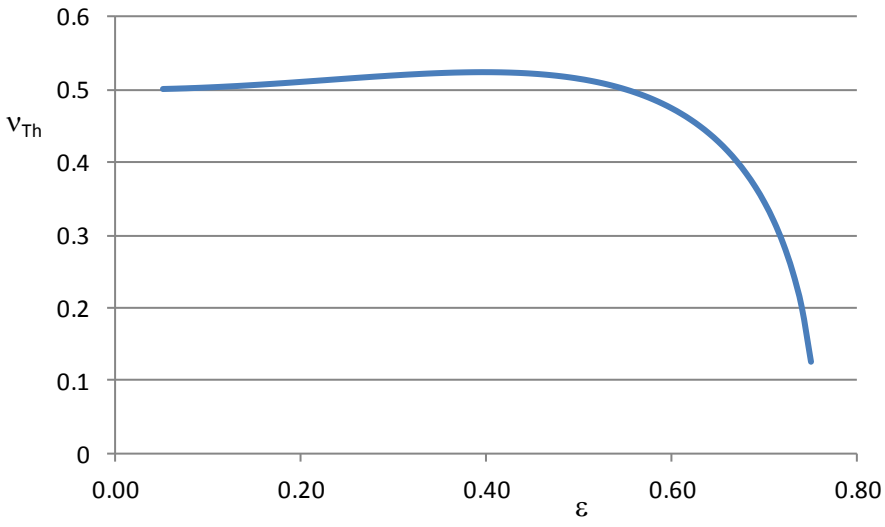

Figure 2-1 Eccentricity versus threshold whirl frequency

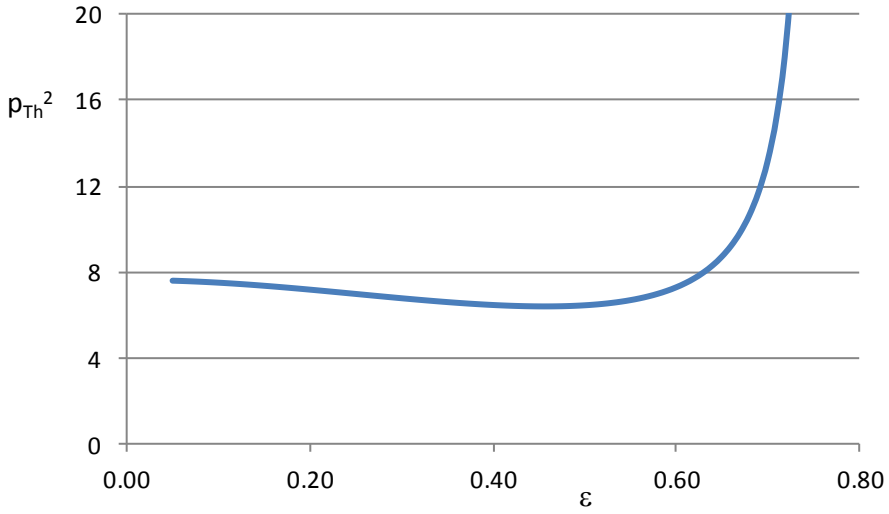

Figure 2-2 Eccentricity versus threshold rotor mass for stability

2.2 Reynolds Equation

To understand performance and characteristics of a gas bearing we first need to understand the pressure profile within the bearing. Figure 2-3 shows the pressure profile and the forces acting between the rotor and the bearing. When the shaft starts to rotate the gas between the shaft and the bearing (top foil) is pressurized by converging-diverging wedge effect also the squeeze effect as discussed earlier.

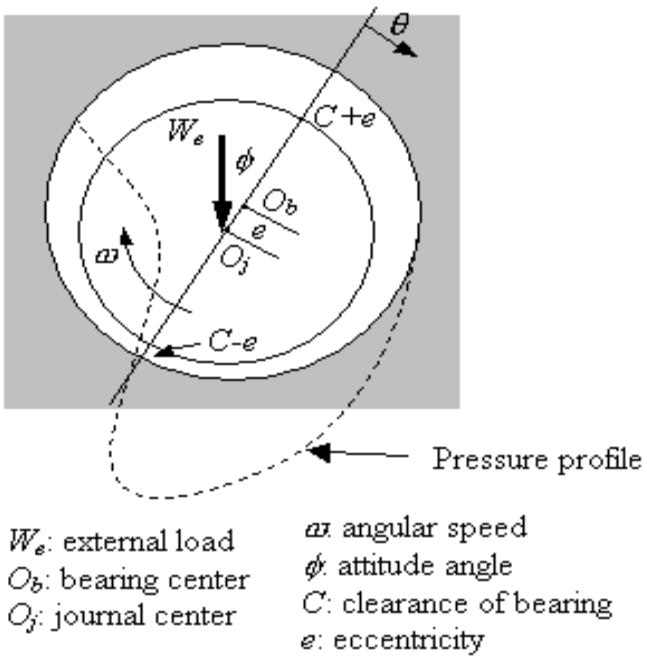

Figure 2-3 Pressure profile of an air foil bearing

The standard governing equation for gas bearings is derived from the Navier-Stoke's equation. A few assumptions are made including thin gas film, no slip boundary condition and negligible curvature. In addition, the gas is assumed to be ideal and under isothermal condition.

$$\frac{\partial}{\partial x}(ph^3\frac{\partial p}{\partial x})+\frac{\partial}{\partial z}(ph^3\frac{\partial p}{\partial z})=6U\mu\frac{\partial}{\partial x}(ph)+12\mu\frac{\partial}{\partial t}(ph) \qquad (2\text{-}2)$$

In the above Reynolds equation, x is the direction of linear surface speed and z the direction of side flow (axial). For all numerical analysis, a non-dimensional Reynolds equation is used for simplicity. Hence, we have

$$\frac{\partial}{\partial\theta}(PH^3\frac{\partial P}{\partial\theta})+\frac{\partial}{\partial Z}(PH^3\frac{\partial P}{\partial Z})=\Lambda\frac{\partial}{\partial\theta}(PH)+2\Lambda\nu\frac{\partial}{\partial\tau_s}(PH) \qquad (2\text{-}3)$$

Where,

$$P = \frac{p}{p_a},\ H = \frac{h}{C},\ \varepsilon = \frac{e}{C},\ \nu = \frac{\omega_s}{\omega},\ \ \Lambda = \frac{6\mu\omega}{p_a}\left(\frac{R}{C}\right)^2 \text{ and } \tau_s = \omega_s t$$

2.3 Simulation Technique

The dynamic performance of a gas bearing system is obtained by simulating the test conditions of the rotor-bearing test rig. There are two major approaches a) Linear perturbation method and b) Orbit simulation method. In linear perturbation method, a small perturbation about the steady state position of the rotor is employed. The perturbation of the first order Reynolds equation gives the corresponding values of stiffness and damping (force coefficients) for the gas bearing. The only limitation encountered in this method is the fact that rotor motion equations are highly non-linear, also the imbalance response can be much higher than the perturbed motion within which solving a linearized Reynolds equation may not be the best option Kim [15]. The other approach (Orbit simulation) suggests the rotor dynamic stability by solving the Reynolds equation (2-3) simultaneously with the journal dynamic equations at each time step. It traces the journal center path over time hence heavy distortions suggest instability. Its advantage lies in the fact that it can also consider molecular rarefaction effects because it solves non-linear Reynolds equation at each time step.

Orbit simulation gives a numerical approximation of the whirl stability at each time step. The below formulation has been derived from [15] for orbit simulation. Considering the journal is aligned axially with the bearing. We have, non-dimensionalized film thickness of the bearing as (refer Figure 2-3 for eccentricity and clearance).

$$H = h / c = \varepsilon_X \sin\theta + \varepsilon_Y \cos\theta \tag{2-4}$$

Now, for a bump type air foil bearing we include bump deflection and the bearing preload factors. Hence, the film thickness becomes,

$$H = h / c = \varepsilon_X \sin\theta + \varepsilon_Y \cos\theta + \mathrm{U}(\theta, \mathrm{Z}) - \mathrm{r}_p \cos(\theta - \theta_p) \qquad (2\text{-}5)$$

Where, C=nominal clearance

$\varepsilon_{X,Y}$ = eccentricity of journal center along X & Y

r_p = bearing preload

θ_p = angular position of the pivot from the leading edge

U (θ) = bump deflection normalized by nominal clearance

The film thickness from (2-5) is used to solve the Reynolds equation (2-3) to obtain the dynamic pressure field. To solve the equation (2-3), $\tau = \omega t$ is used in place of τ_s.

$$\frac{\partial}{\partial\theta}(PH^3\frac{\partial P}{\partial\theta}) + \frac{\partial}{\partial Z}(PH^3\frac{\partial P}{\partial Z}) = \Lambda\frac{\partial}{\partial\theta}(PH) + 2\Lambda\nu\frac{\partial}{\partial\tau}(PH) \qquad (2\text{-}6)$$

Now, the journal is assumed rigid and the equation of journal motions is as follows

$$\frac{d^2\varepsilon_X}{d\tau^2} = \ddot{\varepsilon}_X = \frac{1}{m_r C\omega^2}\left(F_X + m_r u_{im}\omega^2\cos\omega t + m_r g\right) \qquad (2\text{-}7)$$

$$\frac{d^2\varepsilon_Y}{d\tau^2} = \ddot{\varepsilon}_Y = \frac{1}{m_r C\omega^2}\left(F_Y + m_r u_{im}\omega^2\sin\omega t\right) \qquad (2\text{-}8)$$

Where, $F_{X,Y}$ = dynamic bearing reaction forces, m_r =rotor mass,

u_{im} = rotor imbalance radius

In orbit simulation, with the Reynolds equation and journal motion equations, the bump dynamic equation is solved simultaneously. The bump dynamics equation is given by

$$f_b = k_b u + c_b \frac{du}{dt} \tag{2-9}$$

Where, $f_b = pA_0$ =pressure force on bump

k_b = bump stiffness factor coefficient

c_b = equivalent bump viscous damping coefficient

The bump stiffness (k_b) and damping coefficient (c_b) are related as $c_b = \eta k_b / \omega_s$ where, η is the loss factor of each bump. For present simulations a loss factor of 0.2 is used which is derived from well-designed bump foil bearings. Also, The equivalent viscous damping coefficient (c_b) is calculated from the structural loss factor η with the assumption that the motion of elastic foundation is sinusoidal in normal operating conditions.

Below is the bump deflection equation derived from the non-dimensionalized bump stiffness and damping coefficient.

$$P = K_b(\mathrm{U} + \eta \frac{dU}{d\tau_s}) \tag{2-10}$$

Where, $K_b = \frac{k_b C}{p_a A_0}$, $C_b = \frac{C c_b \omega}{p_a A_0} = \frac{\eta}{\nu} k_b$

Further, the viscous damping coefficient is discretized to solve the time varying local bump deflections and the normalized bump deflection equation becomes

$$P^n = K_b U^n + C_b \frac{\Delta U^n}{\Delta \tau} \tag{2-11}$$

Where 'n' is the time index. The first order time derivative approximation gives

$$U^n = \frac{C_b}{C_b + K_b \Delta \tau} U^{n-1} + \frac{\Delta \tau}{C_b + K_b \Delta \tau} P^n \tag{2-12}$$

The first five state variables (ε_X , ε_Y) in time domain results are obtained by solving fourth order Runge Kutta method and then Adams-Bashforth scheme is used. Runge kutta method follows single evaluation of the function i.e. it predicts next state based on a single prior time step whereas Adams-Bashforth scheme uses four evaluations at every time step. The fifth order Adams-Bashforth scheme solves the journal motion equations (2-7) and (2-8) in the time domain. The Reynolds equation is solved by using the displacements and velocities of rotor and top foil obtained from previous time steps.

2.4 Experimental Method

The experiments are carried out on the test rig shown in Figure 3-1. Four eddy current proximity sensors are used to obtain horizontal and vertical rotor vibrations for both bearings at a sampling frequency rate of 80 KHz. A previously developed LABVIEW VI used by Rimpel [16] with few modifications is used for data acquisition. The time-frequency data so obtained is processed and its Fast Fourier Transforms (FFT) is plotted

using MATLAB. The rotor is tested at two feed pressures 4.137 Bars (60psi) and 5.516 Bars (80psi) on two different bearing designs.

TEST FOR BEARING DESIGN I

A previously developed bearing with a single bump foil layer under each Teflon coated top foil is used. The bearing clearance is reduced to match the simulation clearance by adding aluminum foils as shown in Figure 3-2. This bearing is tested at 60 Psi inlet pressure. The rotor is run until the onset of subsynchronous vibrations such that the bottom air feed line can be blocked at subsynchronous vibrations to clearly note the changes in rotor behavior.

TEST FOR BEARING DESIGN II

A new bearing is made with twice the number of bump foils used in previous case but with lower thickness. The resulting bearing has higher stiffness but the clearance is in compliance with the clearance used for simulations. In addition, Tygon flexible tubes are directly glued to the top foil for air injection making use of stainless steel tubes obsolete. The rotor is then tested for subsynchronous vibrations at 80 Psi with a speed increment of 1000 RPM similar to the previous case.

Chapter 3

Test Rig Setup

For the following tests, a previously custom-made Aluminum test rig is used. The cross-sectional view of the test rig is shown in Figure 3-1. The importance of the rig lays in its compactness and robustness as it houses both the Journal HAFB and the motor stator in the same unit. The thrust bearing is attached to the rig on one side and the other side has an open end where a tachometer or a proximity probe can read key phasor signals.

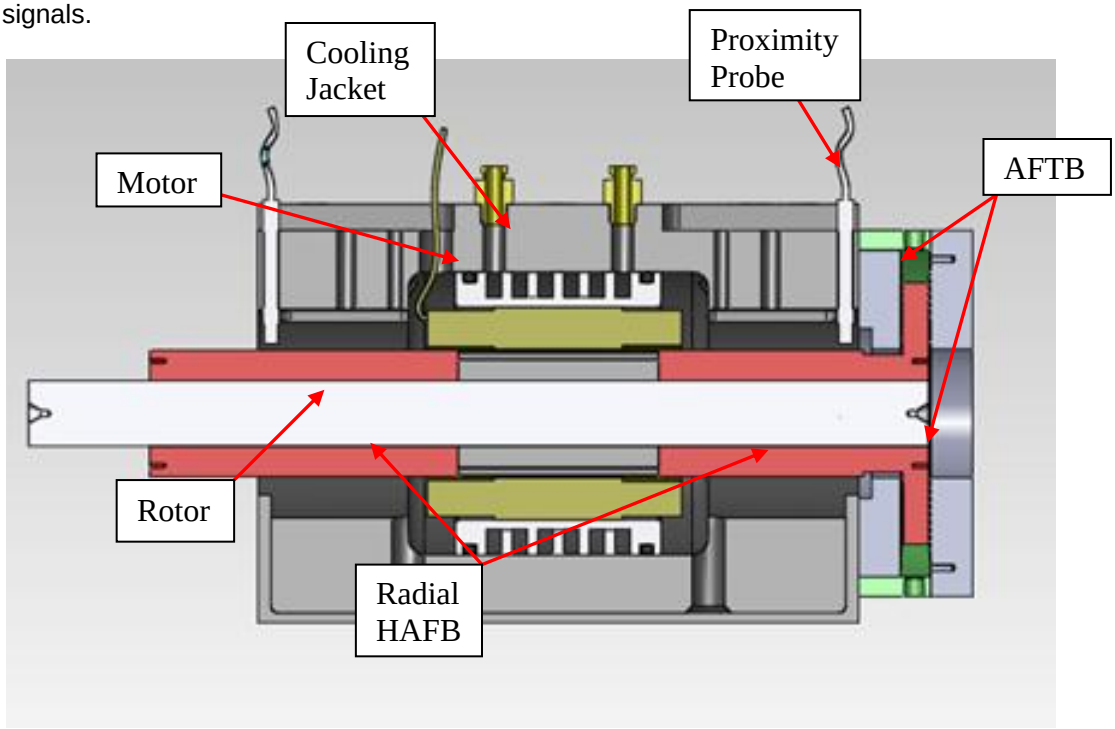

Figure 3-1 Test Rig Setup

3.1 Bearing Design Parameters

As discussed earlier a three-pad bearing was tested for this research. Figure 3-2 shows the bearing assembly for Experimental Test II. Aluminum foil (25 microns in

thickness) is used between the bump foils and the bearing sleeve to reduce the clearance. The lip of the bump foils is glued to the bearing sleeve to avoid displacement. Each top foil has a stainless steel orifice tube attached to them, which find its way out through a slot in the bearing sleeve. The orifice tubes are at 60 ^{o}, 180 ^{o} and 300 ^{o} to vertical in the bearing assembly such that one air injection line sits right beneath the shaft. As mentioned earlier each top foil sits on the bump foils and has its lip sitting in a slot of the bearing sleeve.

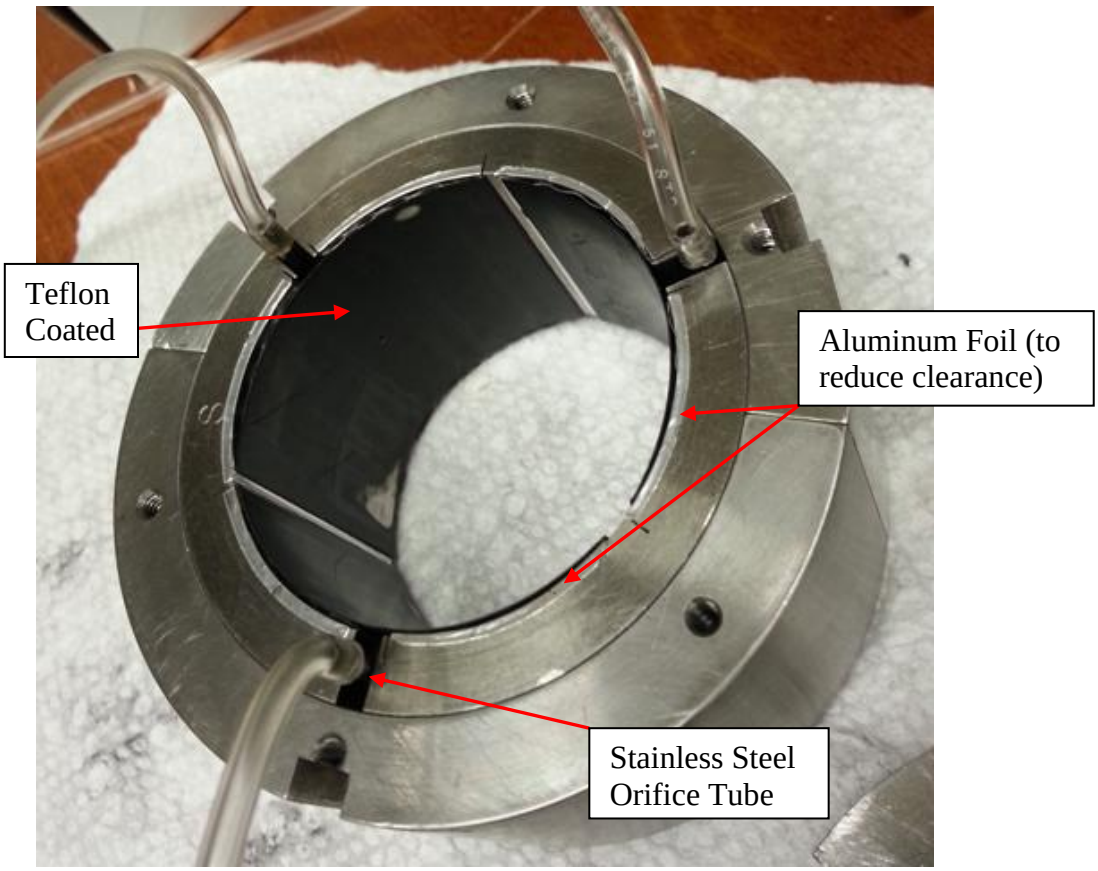

Figure 3-2 Hybrid Air Foil Bearing Assembly

3.2 Manufacturing of HAFB

Most air foil bearing require high level of expertise and attention to detail for their manufacturing due to their intricate designs. The HAFB used here is relatively simple to manufacture. The manufacturing technique for Bearing Design I is similar to the one used by Shetty [17]. The Bearing Design II is different in the way the orifice is attached to the top foil and in the number of bump foils used. The HAFB (Bearing Design II) used has following components:

1. Bearing Sleeve: It acts as a rigid (SS 316) support that houses the top and bump foils. It has thin slots made out of wire Electro Discharge Machining (EDM). These slots are necessary to hold the bump and the top foils as shown in Figure 3-3.

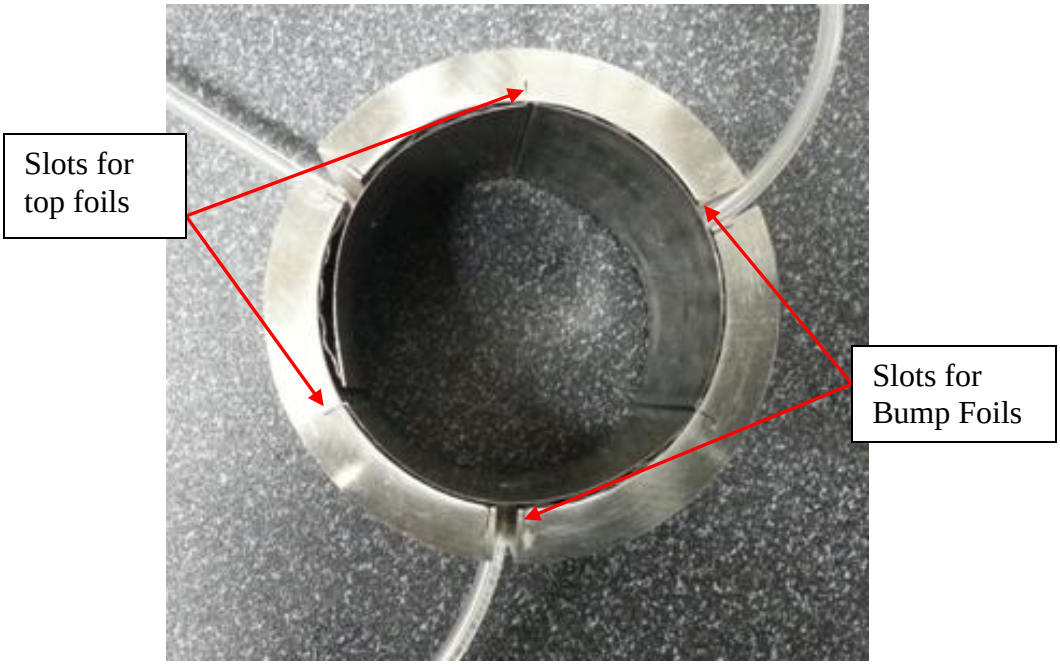

Figure 3-3 Current Hybrid Air Foil Bearing assembly

2. Bump Foils: The new bump foils made are out of a Chromium-Nickel alloy (Inconel 718) with thickness 0.0762 mm. To increase the stiffness, two bump

foil layers are used instead of one and hence there are four bump foils beneath each top foil. The bump foil is first pre-formed on a jig (used in [17]) using a hydraulic press and then formed again (on jig shown in Figure 3-4) to get the desired bump height distribution. The load concentration for the previous jig (used in [17]) is at the center (near third bump) whereas, the highest load concentration is desired at the first bump (from the lip section), necessary for the preload.. For the present bearing, the bump at the lip section has to be nearly 10 microns higher than the bump at the free end to allow proper bearing preload.

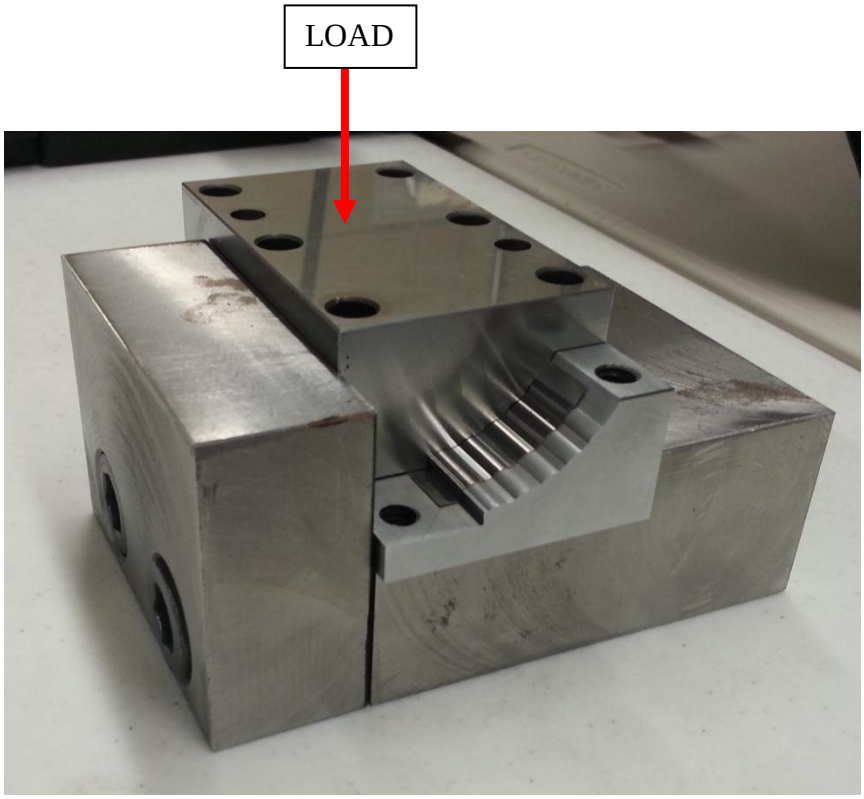

Figure 3-4 Second stage forming jig

3. Top Foils: There are three top foils per bearing of thickness 0.1524 mm. The top foils are made in the same way as the bump foils, they are formed in a forming jig under a pressure of eight tons and then heat treated. The top foils are then drilled with 1 mm hole to accommodate an orifice tube of 0.083 in OD. The previous design of soldering the stainless steel orifice tube was not accepted due to the blockage of the orifice hole with the solder. There was always a possibility of the orifice tube injecting solder particles during bearing operation. Hence, it was decided to stick the Tygon tubing directly to the top foil with the help of super glue. Both the designs are shown in the Figure 3-5.The other difference between the previous and the present design lays in the coating of the top foil. The current top foils are not coated with Teflon due to time constraints.

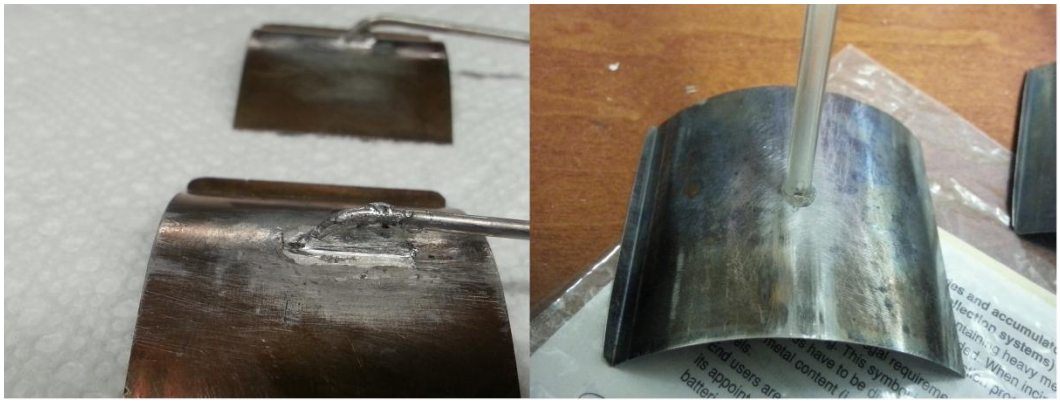

Figure 3-5 Orifice attachment

At speeds above 30000 RPM, stability of the rotor becomes prime concern. Kim [15] showed that in a three-pad bearing configuration, preload plays a key role for rotor stability. The bearing designed here has a higher bump height at the lip area (the bump foil section that sits into the slots) and it gradually decreases towards the free end. The preload and the clearance of an air foil journal bearing are related by

$$R_p = 1 - \frac{C_{SB}}{r_p + C_{SB}} \tag{3-1}$$

Where, R_p =Non-dimensionalized preload,

C_{SB} =Minimum clearance (between top foil and rotor)

r_p = Preload (distance between top foil center and rotor center)

Due to the relation between preload and the clearance and their role in rotor stability it was important to measure each bump height individually. Below is the bump height distribution for front bearing. The bump height for the present experiments were carried out by using a dummy shaft (50 microns less in diameter to the original shaft) in the bearing assembly as shown in Figure 3-6 to allow uniform pressure on the bumps.

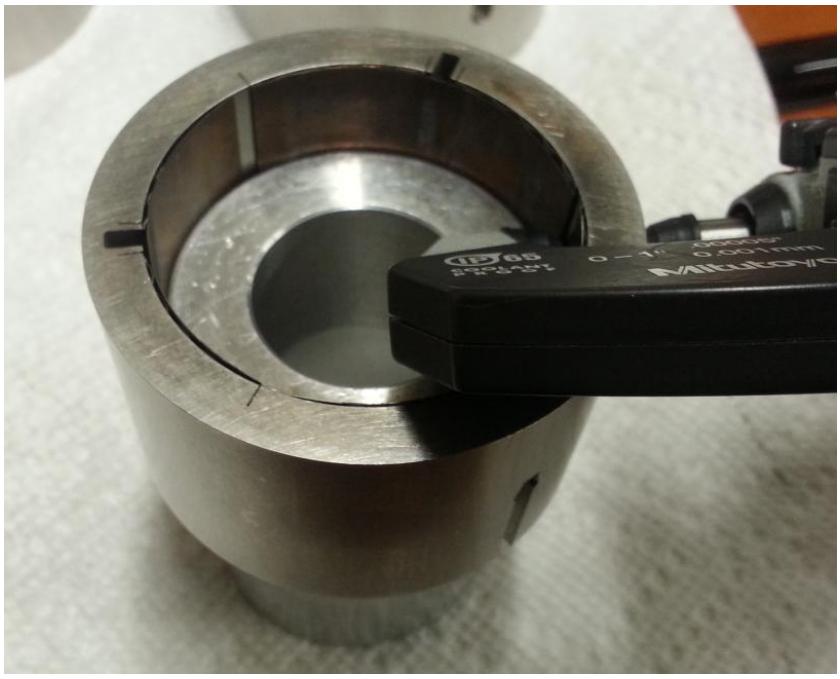

Figure 3-6 Bump height measurement method

Trial 1 and Trial 2 were carried out at different locations of the bearing. The bump heights shown in Table 3-1 and

Table 3-2 are inclusive of the bearing sleeve thickness (0.2575 in) and the top foil thickness together. Below is the bump height distribution for the front bearing.

Table 3-1 Bump height distribution for front bearing

	TRIAL 1 (All dimensions in inches)					
	Bump 1	Bump 2	Bump 3	Bump 4	Bump 5	Bump height difference
Bump Foil 1	0.28535	0.28345	0.28305	0.2838	0.2813	**0.00405**
Bump Foil 2	0.28305	0.283	0.2832	0.28235	0.28015	**0.0029**
Bump Foil 3	0.28625	0.2859	0.28495	0.285	0.2822	**0.00405**
Bump Foil 4	0.2835	0.28375	0.2818	0.28225	0.28045	**0.00305**
Bump Foil 5	0.286	0.28615	0.28565	0.28615	0.2825	**0.0035**
Bump Foil 6	0.2849	0.2847	0.2845	0.2825	0.27995	**0.00495**
	TRIAL 2 (All dimensions in inches)					
	Bump 1	Bump 2	Bump 3	Bump 4	Bump 5	Bump height difference
Bump Foil 1	0.2829	0.2814	0.28085	0.2813	0.27935	**0.00355**
Bump Foil 2	0.2834	0.28405	0.28345	0.28265	0.27905	**0.00435**
Bump Foil 3	0.28295	0.2832	0.283	0.28285	0.2811	**0.00185**
Bump Foil 4	0.2837	0.28285	0.28355	0.2827	0.28105	**0.00265**
Bump Foil 5	0.28265	0.28245	0.2825	0.28245	0.2799	**0.00275**
Bump Foil 6	0.2843	0.28425	0.2829	0.28325	0.28025	**0.00405**

The bump height difference in the last column of Table 3-1 and Table 3-2 corresponds to the difference in height of bump at the lip section (fixed) to the bump at the free end. The positive bump height difference further boosts non-uniform bearing clearance. In spite of special care taken to obtain the desired bump height distribution, some amount of uncertainty prevails. Various combination of bump foils were tried to get

closest bump height distribution. The slight uncertainty can be ignored as long as a positive bump height difference is obtained. Similar positive bump height difference is obtained for the rear bearing as shown below.

Table 3-2 Bump height distribution for rear bearing

	TRIAL 1 (All dimensions in inches)					
	Bump 1	Bump 2	Bump 3	Bump 4	Bump 5	Bump height difference
Bump Foil 1	0.28405	0.2826	0.2825	0.2817	0.27945	**0.0046**
Bump Foil 2	0.28165	0.2827	0.28275	0.28295	0.2804	**0.00125**
Bump Foil 3	0.2826	0.2841	0.2818	0.2816	0.27985	**0.00275**
Bump Foil 4	0.28185	0.2835	0.28375	0.2824	0.281555	**0.000295**
Bump Foil 5	0.2832	0.2824	0.2815	0.2822	0.28085	**0.00235**
Bump Foil 6	0.28205	0.2836	0.284	0.28325	0.27815	**0.0039**
	TRIAL 2 (All dimensions in inches)					
	Bump 1	Bump 2	Bump 3	Bump 4	Bump 5	Bump height difference
Bump Foil 1	0.2823	0.2834	0.28255	0.2822	0.2799	**0.0024**
Bump Foil 2	0.2817	0.28215	0.2819	0.2816	0.27895	**0.00275**
Bump Foil 3	0.28495	0.28395	0.2826	0.2831	0.2823	**0.00265**
Bump Foil 4	0.2841	0.28305	0.2827	0.28105	0.2788	**0.0053**
Bump Foil 5	0.28295	0.2841	0.2835	0.28295	0.2817	**0.00125**
Bump Foil 6	0.28315	0.2827	0.2816	0.28275	0.2788	**0.00435**

3.3 Manufacturing of AFTB

As already discussed in section 1.3 of Chapter 1, a novel thrust bearing model has been fabricated for the present research. The bearing was recently developed at Microturbomachinery and Energy Systems Laboratory at University of Texas at Arlington by Kim and Lee [8]. A completely assembled thrust bearing is shown in the Figure 3-7. It consists of three parts A) the top foil B) the bump foil C) and the backing plate. The top

foil is made up of stainless steel 316 of thickness 0.127 mm and has some curvature to assist in hydrodynamic film lift. The top foil is fabricated on an Electro Discharge Machine (EDM) and each thrust bearing has 6 top foils. The top foils are spot welded at the leading edge as shown below.

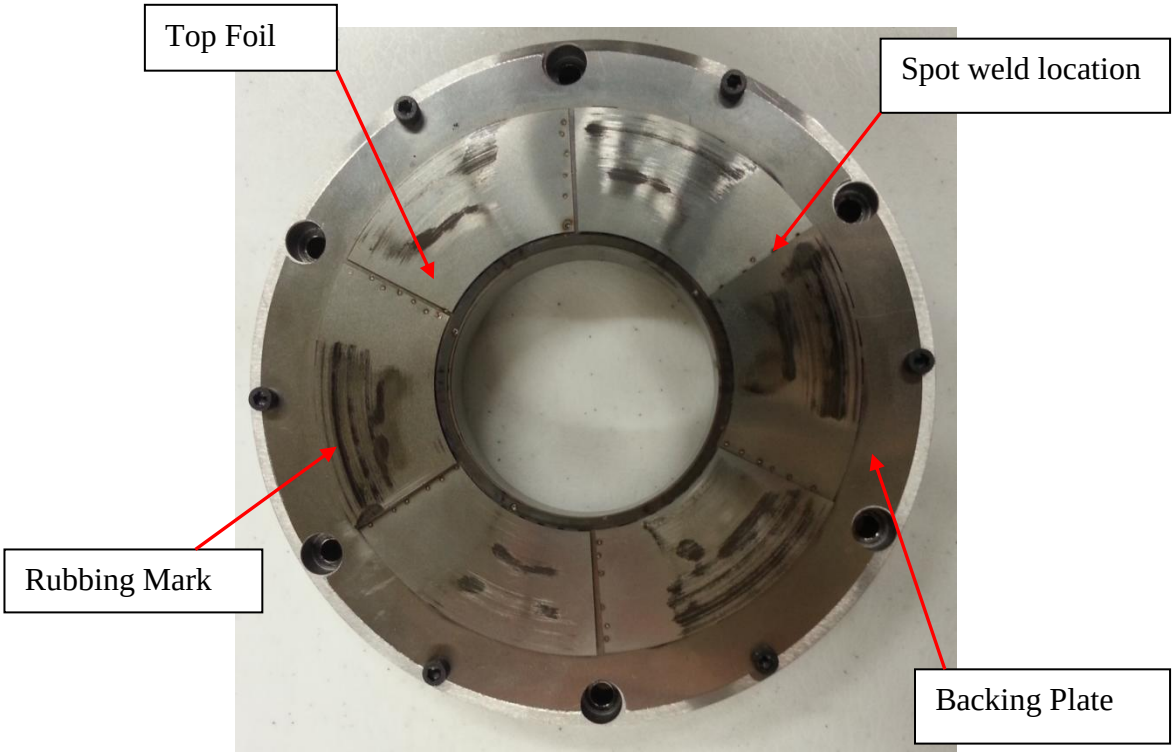

Figure 3-7 AFTB Assembly

Exactly beneath the top foils is the bump foil which is formed in a jig as shown in Figure 3-8 with a pressure of about 8 ton and is then heat treated. The two initial bump strips are cut off to accommodate taper contour of the top foil. It is then spot welded to the backing plate. The radial arrangement of the bump structure helps in better cooling of the thrust bearing. The bump foil is made of Inconel 718 of thickness 0.127mm and with average thrust bearing height (includes top foil, bump foil and backing plate) of 0.88 mm. The top foils and the bump foil are spot welded to the backing plate and it acts as the support medium to hold them together.

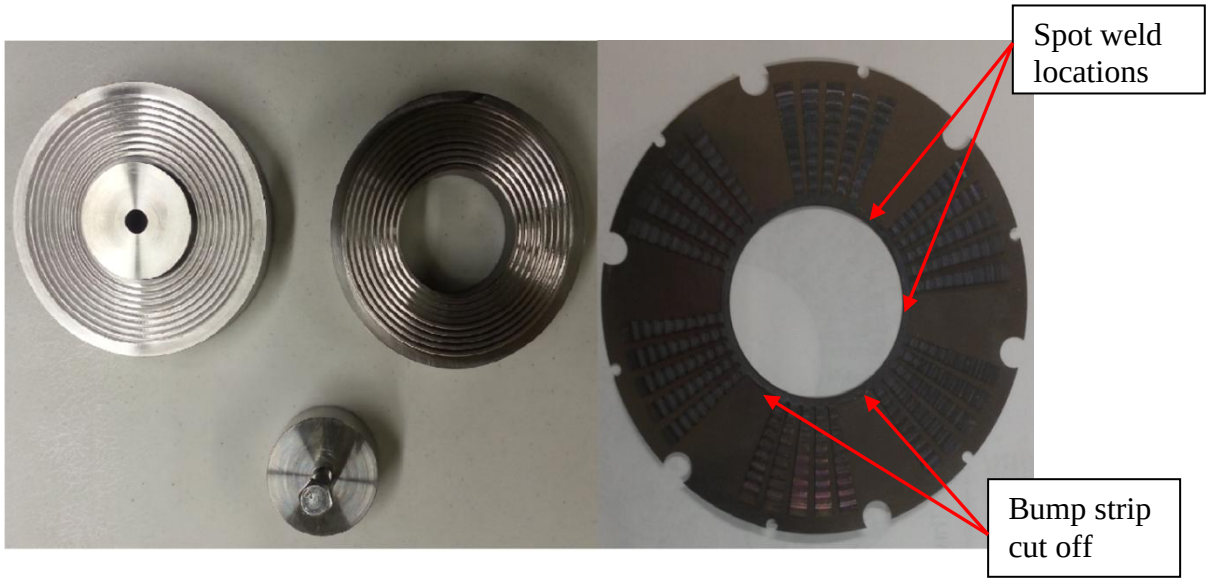

Figure 3-8 Bump foil Jig (left) and bump foil spot welded (right)

As mentioned earlier, clearance is a very important criterion in the air foil bearings. To understand the procedure followed to obtain thrust clearance lets first look at the cross-sectional solid model assembly of the thrust pad bearing.

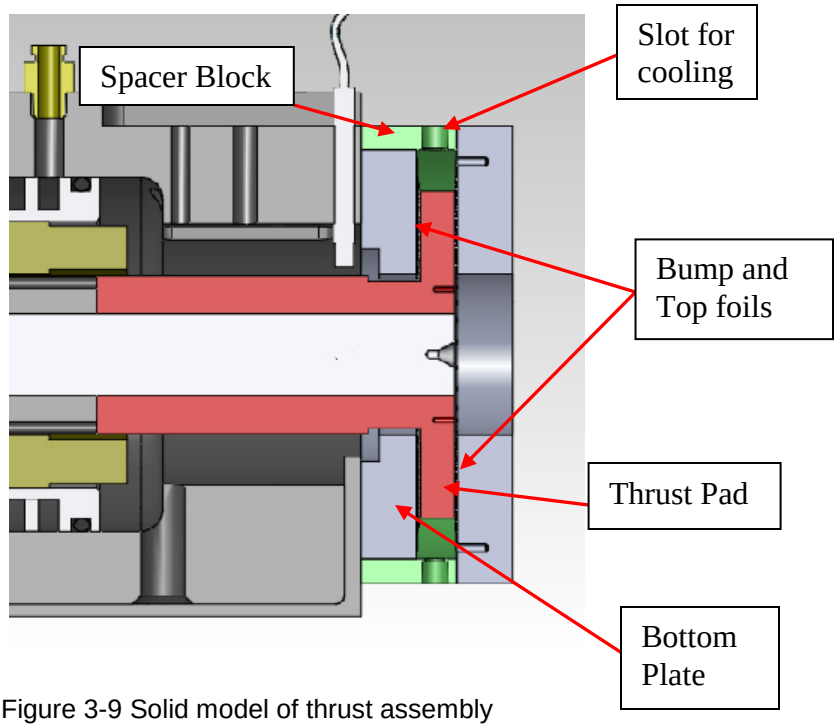

Figure 3-9 Solid model of thrust assembly

A thrust pad dummy is used on top of the bump foil on a flat surface to measure the bump height with the help of a height gauge. The total clearance is found by subtracting the bottom plate thickness, bump foil height, the top foil thickness and the thrust pad thickness from the spacer block thickness. The Table 3-3 shows the bump height and clearance for both sides of the thrust bearing.

Total clearance = Spacer Block – [Bottom Plate + (Plate layer + Bump height+ Top foil) $_{front}$ + (Plate layer + Bump height+ Top foil) $_{rear}$]

Table 3-3 Thrust bearing clearance

Thrust Bearing	Parts	Height(mm)
	Spacer Block	27.95083333
	Bottom Plate	16.22116667
Counterclockwise(front pad)	Plate Layer	0.810683333
	Bump Height	
	Top Foil	
	Thrust Pad	10.0055
Clockwise(rear pad)	Top Foil	0.80899
	Bump Height	
	Plate Layer	
Total Clearance for both disc sides = Spacer block-(Bottom Plate + CCW + CW)		**0.104**

Chapter 4

Results and Discussions

Orbit simulations are carried out for the bearing at different pressure conditions, with all air feed lines open and only the top two air feed lines open (keeping the bottom air feed line blocked). Higher computational grid points are used for cases that require higher simulated steady state response to converge in the time domain. The general parameters considered for the simulations are shown in the Table 4-1.

Table 4-1 Bearing Simulation Parameters

Bearing Radius R(mm)	24.5
Bearing axial Length L(mm)	37.5
Nominal Clearance C(mm)	0.07
Number of bumps in a Pad	11
n	22
m	16
Number of Pad	3
Rotor Mass (kg)	2.42
Imbalance in (mg-mm)	2500
Bump stiffness along length	2.09E+06
Loss Factor η	0.2
Bearing Preload Rp (mm)	0.03
Top foil thickness (mm)	0.1524
Radius of orifice (mm)	0.5
Supply Pressure (Bar)	4.14, 5.52

4.1 Simulation Results

The objective of the research is to see the beneficial effects of rotor loading by controlling air feed at instability inception. The tests were first carried out to register the changes in subsynchronous vibrations when the bottom air line was turned off, maintaining the pressure from other two air lines. Below is the simulation result for a

horizontal probe (direction orthogonal to rotor load) with all air feed lines operative at 60 Psi (4.14 Bar).

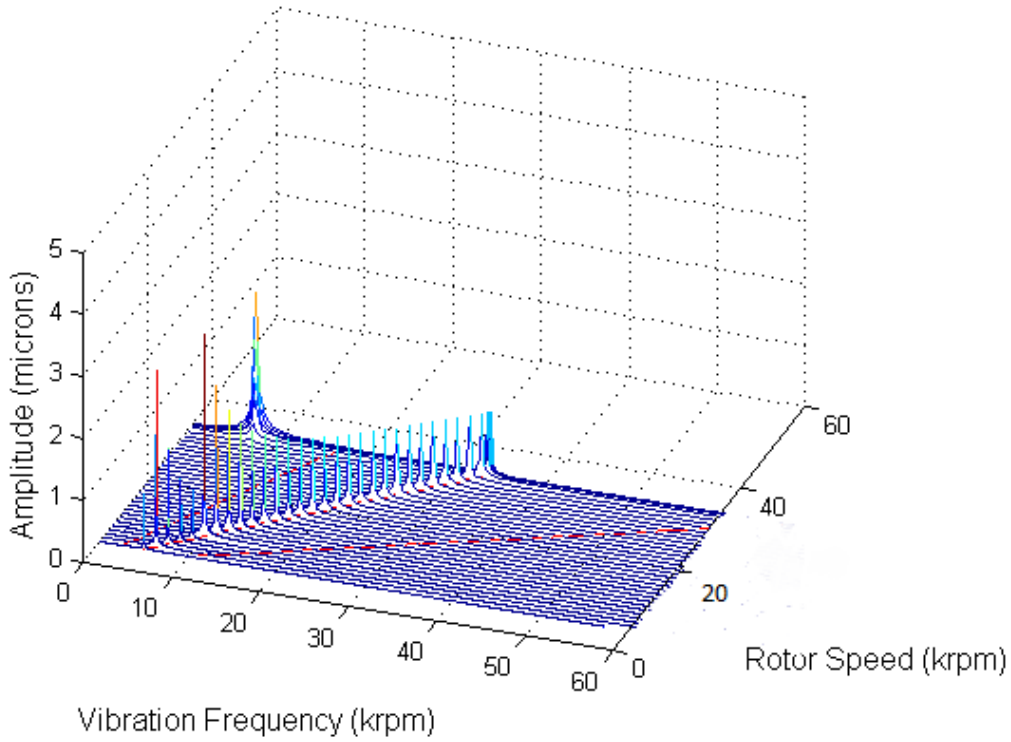

Figure 4-1 Simulation at 60 Psi (all air feed lines operative)

The waterfall plot above depicts the amplitudes (Y-Axis), Vibration Frequency (X-Axis) and the rotor Speed (Z-Axis). The synchronous vibrations show a sudden rise in amplitude at the critical speed (ranging 5000 -10000 RPM) and thereafter follow steady amplitude as expected. Also, it can be seen that the subsynchronous vibrations start at a speed of 33000 RPM but the rise of subsynchronous amplitude observed is quite rapid. Within a speed range of 500 RPM the amplitude rises up to 2 microns and at speeds higher than that the bearing fails (at 34000 RPM shaft is out of control).

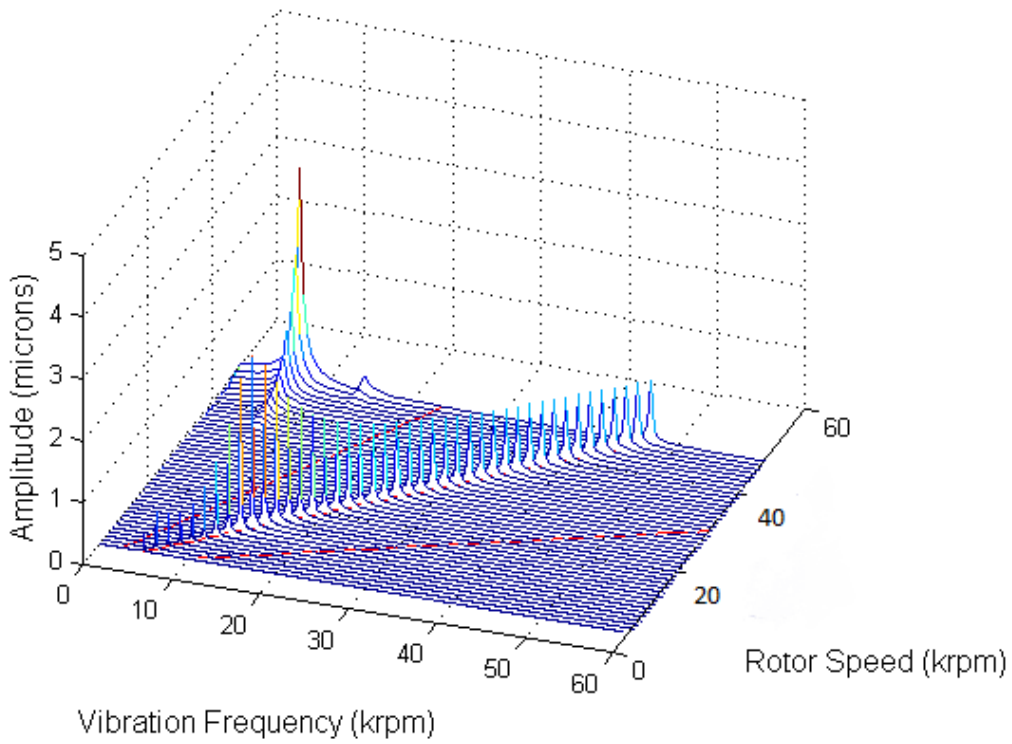

Figure 4-2 Simulation at 60 psi (Bottom air line blocked)

To compare the effect of air feed loading, another simulation was carried out with the same supply pressure of 60 psi (4.14 Bar) but no bottom air feed line. A delay is seen in the critical speed as well as the subsynchronous vibrations. The onset of subsynchronous vibration is observed at around 36000 RPM (Figure 4-2). Moreover, at speeds as high as 47000 RPM the subsynchronous vibration reaches slightly over 3 microns in amplitude. Though the onset of subsynchronous frequency for all air lines open and the bottom air line closed show a slight difference of about 3000 RPM, the case II (bottom air line blocked) suggests a more stable rotor due to the fact that the rise in subsynchronous amplitudes is not as rapid as with all air feed lines operative. In this case (no bottom air feed line) the subsynchronous vibrations are bound to a speed range of

8000 RPM before it grows large also the amplitude is less than 1 micron for speeds ranging from 36000 RPM to 44000 RPM.

With similar parameters, simulations were carried out for a higher inlet pressure of 80 psi (5.52 Bar). Figure 4-3 shows the case for all lines open. The initial rise in the synchronous vibrations is attributed to the critical speed of system. The subsynchronous vibration starts at speeds around 33000 RPM and goes all the way up to 36000 RPM (amplitude rises to 4 microns).

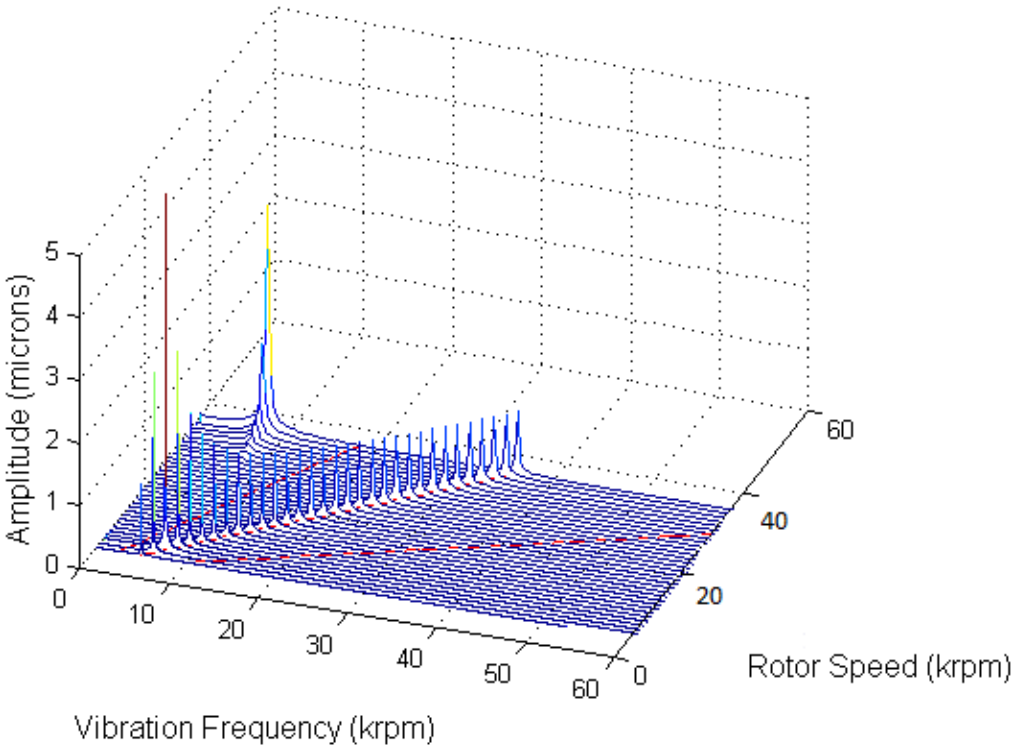

Figure 4-3 Simulation at 80 Psi (All air lines open)

The case with bottom air line blocked at 80 Psi is shown in Figure 4-4. A very similar trend as seen with 60 Psi is observed. The critical amplitudes are lower and are witnessed at higher speeds. Also, the subsynchronous vibrations start at nearly the same speed but in case II (bottom air line blocked) it is bound to a longer speed range

suggesting more stable rotor as noted earlier. The subsynchronous starts at around 40000 RPM and goes all the way up to 50000 RPM where the amplitude rise is nearly 3 microns.

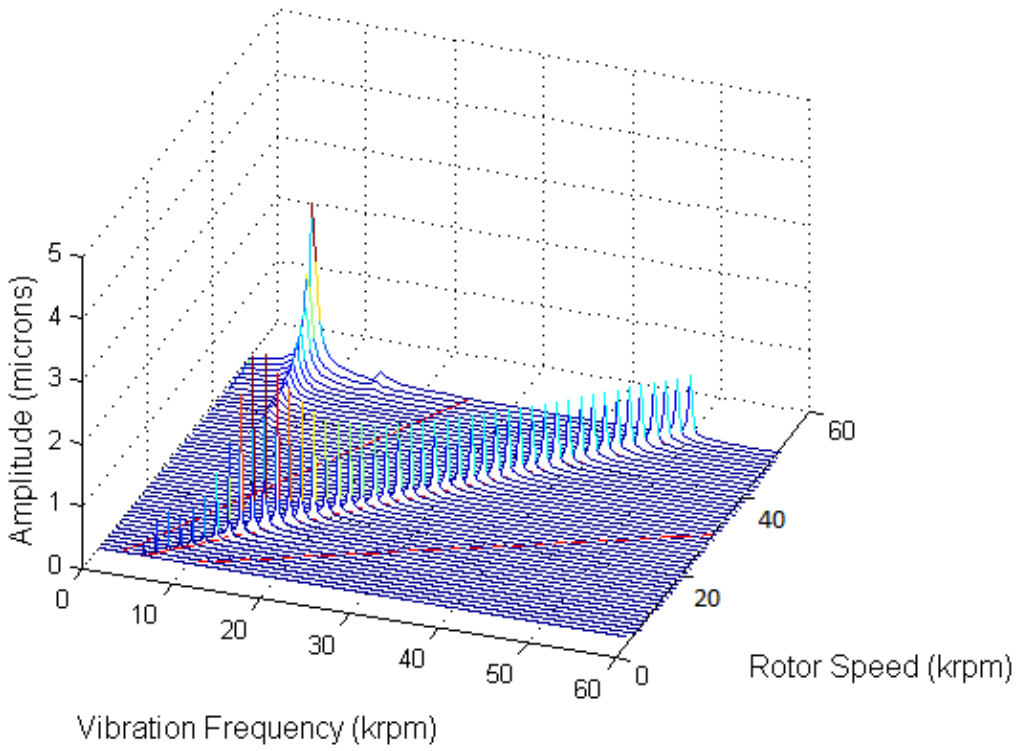

Figure 4-4 Simulation at 80 Psi (bottom air line blocked)

4.2 Experimental Results

The simulation results obtained above clearly predict the usefulness of blocking bottom air feed line, as it delays the onset of subsynchronous vibrations and pushes the shaft to higher stability. The following experiments are performed on a rotor supported by HAFB and AFTB with similar test conditions as of the simulation test parameters. The experimental tests are necessary to validate the simulation test outcome.

The most important criteria of a gas bearing design for stability at high speed are its preload and the clearance as already discussed. For a gas bearing, if the clearance is too tight it might lead to thermal degradation and if the clearance is too large the load characteristics are compromised. Initial test runs were carried out to find the optimum clearance for the thrust bearing. The rotor was run up to 20000 RPM under different shim sizes to manipulate the clearance. The clearance is maintained with a shim added of thickness 0.006 in.

4.2.1 Experimental test I

The first set of experiment is carried out on a previously developed bearing by Shetty[17]. The rotor is run to a speed until subsynchronous vibrations are witnessed. Once the subsynchronous vibrations are seen the bottom air injection line is slowly closed in steps for both front and rear bearing. The data is recorded (Figure 4-5) for both cases (all air lines open at 60 Psi and only bottom air line blocked) but no significant change is observed in the rotor characteristics. The reason being the top two open air feed lines could not create enough load on the shaft due to high clearance. The previous grinding and recoating of the shaft had resulted in an increase of the clearance (nearly 50 microns diametrically). Hence, it was decided to reduce the journal bearing clearance as well by adding aluminum foils (discussed in later section). The journal bearing clearance was modified in such a way that it was in close approximation to the clearance used in the simulations (70 microns).

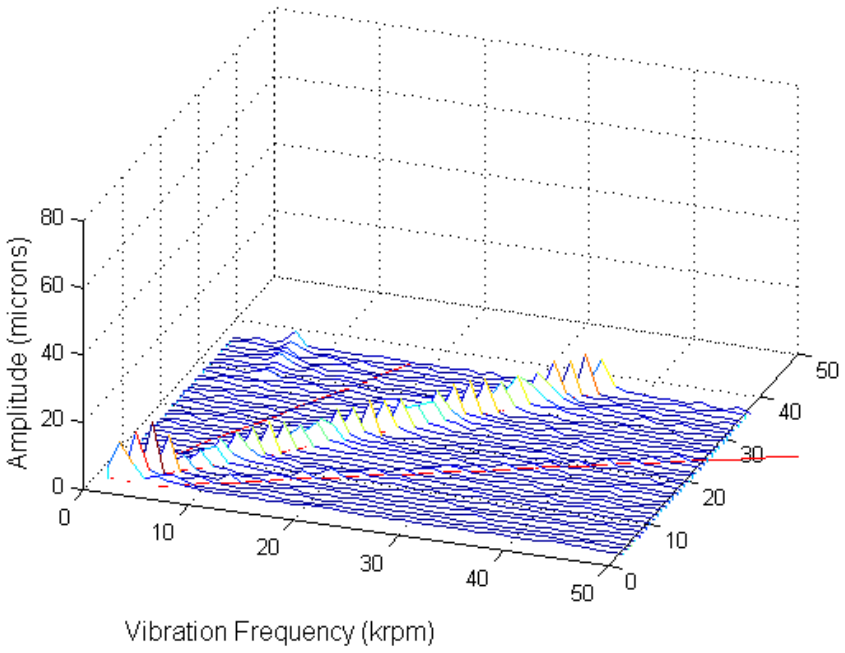

(A)

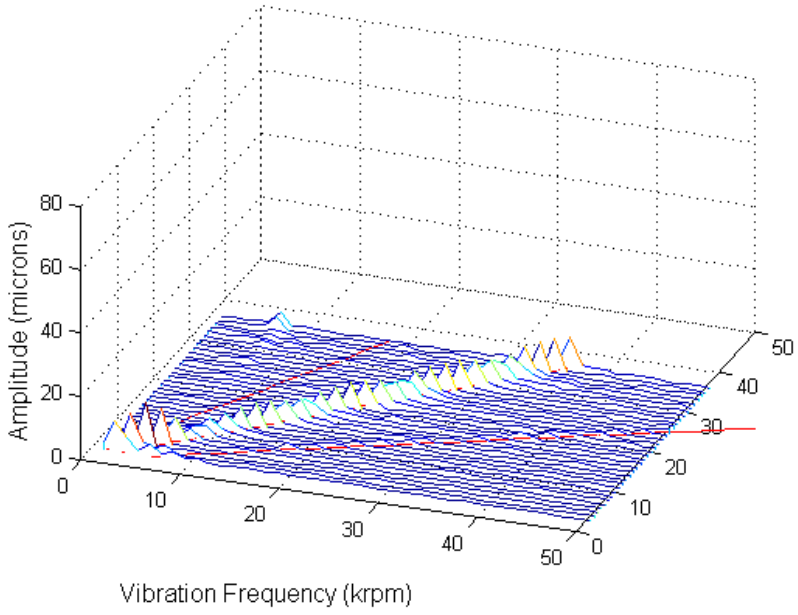

(B)

Figure 4-5 Front Bearing plot for Test I (A) Horizontal probe (B) Vertical probe

4.2.2 Experimental Test II

The subsequent bearing was checked for rubbing and slight unevenness in the top foil profile also its clearance was reduced by 50 microns with the addition of aluminum foil beneath the bump foil layer (Figure 3-2). Again, the intention was to witness subsynchronous vibrations at 60 Psi inlet pressure and then block the bottom air injection line to record the changes in rotor behavior. However, the optimum clearance and a smooth top foil profile resulted in a very stable rotor. Figure 4-6 shows the plots for horizontal and vertical probes of the front bearing.

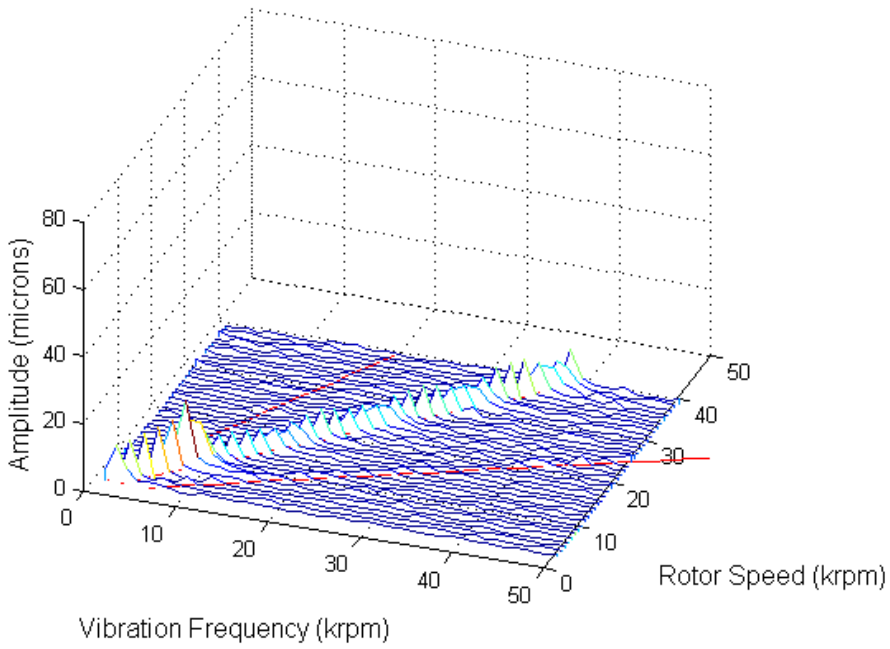

(A)

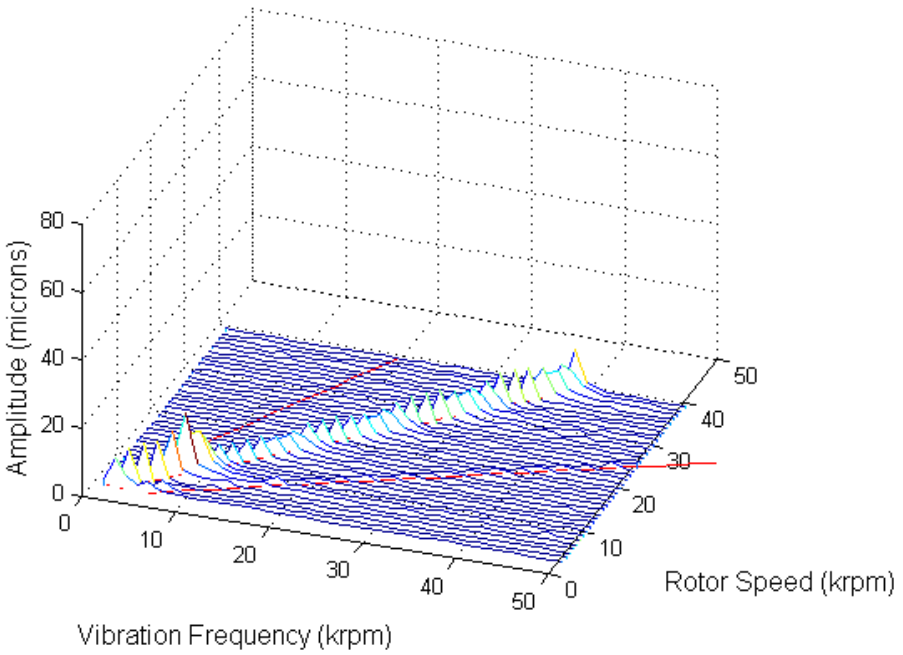

(B)

Figure 4-6 Front Bearing plot for Test II (A) Horizontal probe (B) Vertical probe

The bearing showed no sign of subsynchronous vibrations even at 39000 RPM as compared to 34000 RPM from the simulation results but unfortunately the front bearing was damaged at speed above that due to coating failure. The failure mechanism is discussed in Appendix B (Shaft Failure).

4.2.3 Experimental Test III

The next set of experiment was performed with higher cooling at 80 psi (5.516 Bar) on a newly developed bearing (Bearing Design II mentioned under section 2.4) with higher stiffness but nearly the same clearance. In addition, the shaft was hard chrome plated with a higher thickness (0.01 in) to avoid shaft failures at high speeds [18]. Following the changes in the bearing and shaft, the air flow rate was also carefully adjusted for the new bearing by trying different top foils arrangements. The idea was to

get uniform mass flow rate from each top foil. The blue marks in the Table 4-2 shows mass flow rates of the top foil combination used in the assembly. For both bearings, the top foils with lowest mass flow rate were used as the bottom pad in the bearing because that would be eventually blocked at subsynchronous vibrations.

Table 4-2 Flow Rates before assembly

	Flow Rate(l/min)			
Front Bearing	Top Foil 1	Top Foil 2	Top Foil 3	Total
	5.9	3.8	6.3	16
	6.1	5	4.2	15.3
	6.1	5.4	2.4	13.9
	Flow rate(l/min)			
Rear Bearing	Top Foil 1	Top Foil 2	Top Foil 3	Total
	4.8	5.9	6.2	16.9
	3.7	4.2	6.5	14.4
	4.3	6.5	6.5	17.3

In the complete assembly, the mass flow rate was again tested to match the requirements because the rotor weight is chiefly on the bottom pads of both bearing and that creates non-uniform flows. In the Table 4-3 the blue marks the mass flow rate from the bottom pads of the bearings. The difference is slight in the rear bearing and hence it was ignored.

Table 4-3 Flow rate after assembly

	Flow Rate(l/min)		
Front Bearing	Top Foil 1	Top Foil 2	Top Foil 3
	9.9	9.7	7.7

Rear Bearing	Flow Rate(l/min)		
	Top Foil 1	Top Foil 2	Top Foil 3
	9.6	8.4	13.6

The new bearing developed was again tested for subsynchronous vibrations. The bearing showed remarkable results (DN of slightly over 2.3 Million) with no sign of instability even at 48000 RPM, which is much higher than the simulation predictions. The Figure 4-7 shows the cascade plots for front bearing.

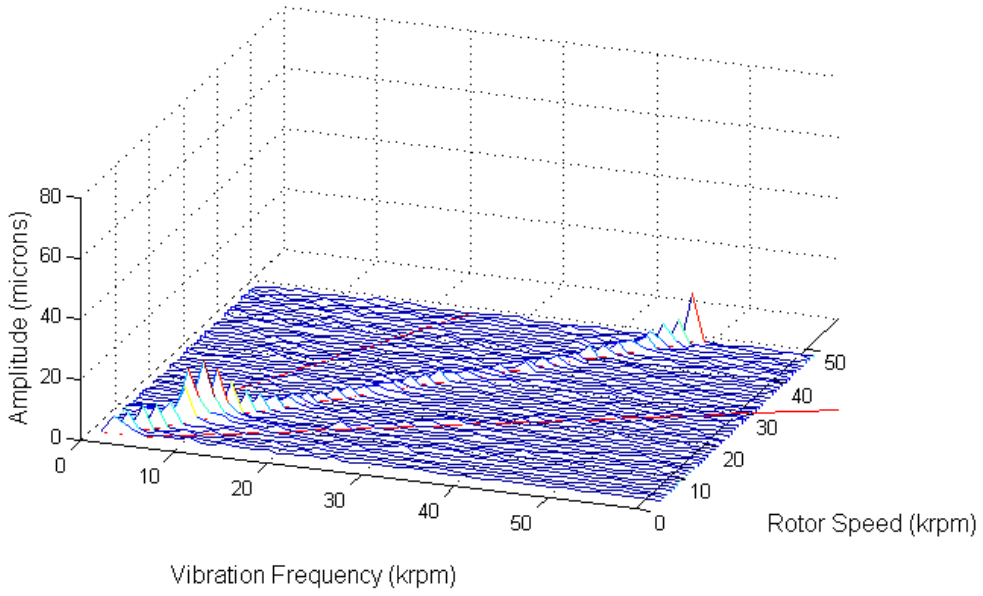

(A)

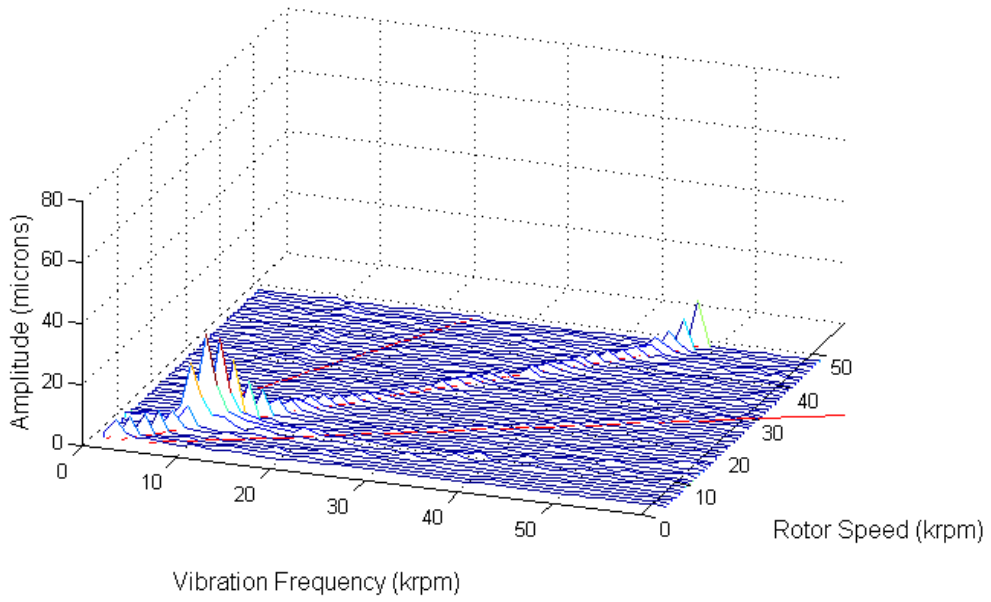

(B)

Figure 4-7 Front Bearing plot for Test III (A) Horizontal probe (B) Vertical probe

4.2.4 Experimental Test IV

Following the second rotor damage, a new front bearing was developed with the same parameters as the previous one (i.e. double bump layer). The air flow rate was adjusted to get a uniform air flow from all the three air foils similar to the previous case. After the assembly, the air feed lines showed slightly deviated values of mass flow rate due to the rotor weight on the bottom foils. The air flow rate for both the bearings is shown below.

Table 4-4 Flow rate after assembly II

	Flow Rate(l/min)		
Front Bearing	Top Foil 1	Top Foil 2	Top Foil 3
	9.4	10.7	12.2

Rear Bearing	Flow Rate(l/min)		
	Top Foil 1	Top Foil 2	Top Foil 3
	9.2	8.8	14.5

The new bearing has onset of subsynchronous frequency at 35000 RPM. The bottom air feed line was blocked for both the bearings to test the effect of controlled air injection. The test was performed for a range of speed, from 35000 RPM to 40000 RPM. For each speed, blocking the bottom air feed line reduced the amplitude of subsynchronous vibration. Later, the bearing was tested at 45000 RPM to witness any higher amplitude of subsynchronous vibrations. Figure 4-8 shows the amplitude versus frequency plot for speeds 35000 RPM, 40000 RPM and 45000 RPM for both conditions (all air feed lines on and bottom air feed line blocked) at 60 Psi. Figure 4-8 (A), depicts a subsynchronous vibration at around 9500 RPM (or 158 Hz in blue color) but when the bottom air line is blocked (red color), the subsynchronous frequency disappears. A similar trend is observed at speeds 40000 RPM and 45000 RPM (Figure 4-8 (B) and (C)). Not much change is seen in synchronous vibrations.

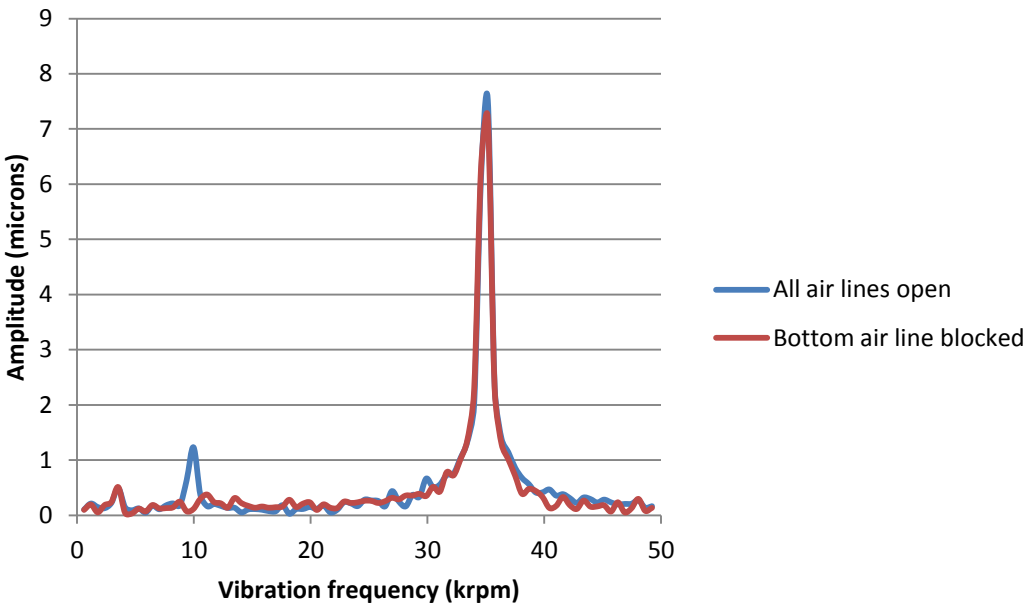
Amplitude (microns)
0
1
2
3
4
5
6
7
8
9
0
10
20
30
40
50
Vibration frequency (krpm)
All air lines open
Bottom air line blocked

(A)

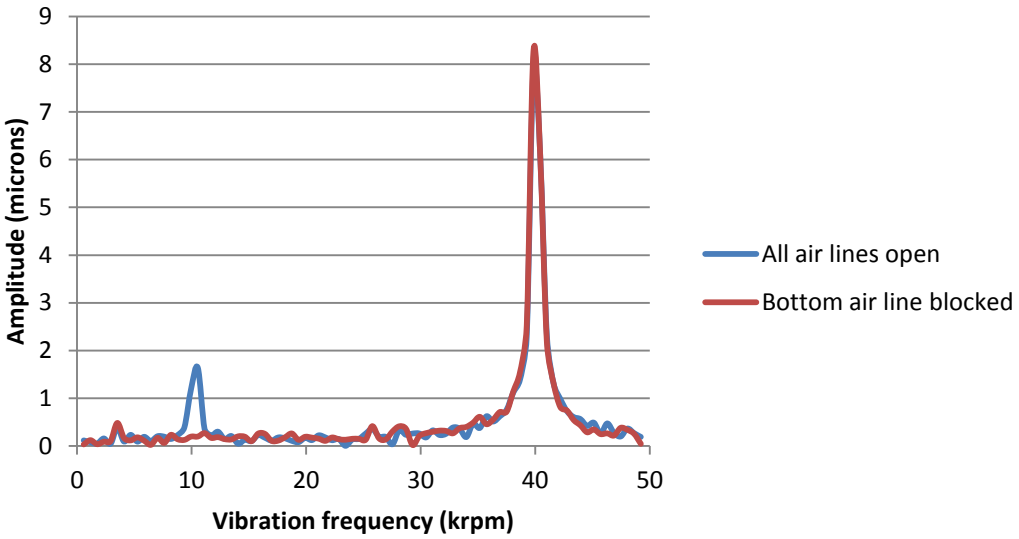
Amplitude (microns)
0
1
2
3
4
5
6
7
8
9
0
10
20
30
40
50
Vibration frequency (krpm)
All air lines open
Bottom air line blocked

(B)

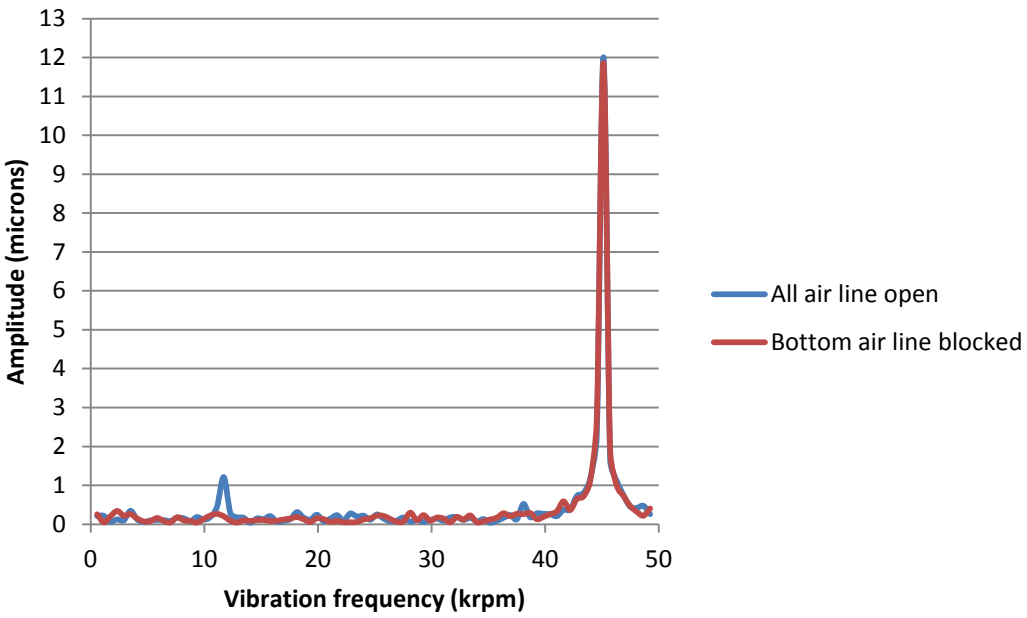

(C)

Figure 4-8 FFT Plots at 60 Psi (A) 35000 RPM (B) 40000 RPM (C) 45000 RPM

Figure 4-9 shows the result for 80 Psi pressure. The subsynchronous amplitude disappears for all speed ranges from 35000 RPM to 40000 RPM, when the bottom air feed line is blocked. The bearing was also tested at 45000 RPM to monitor the growth in the subsynchronous amplitude. Further, tests beyond 45000 RPM were not performed to avoid any rotor damage resulting from high synchronous amplitudes (high synchronous amplitudes at high speeds is assumed to be driven by coating related issues).

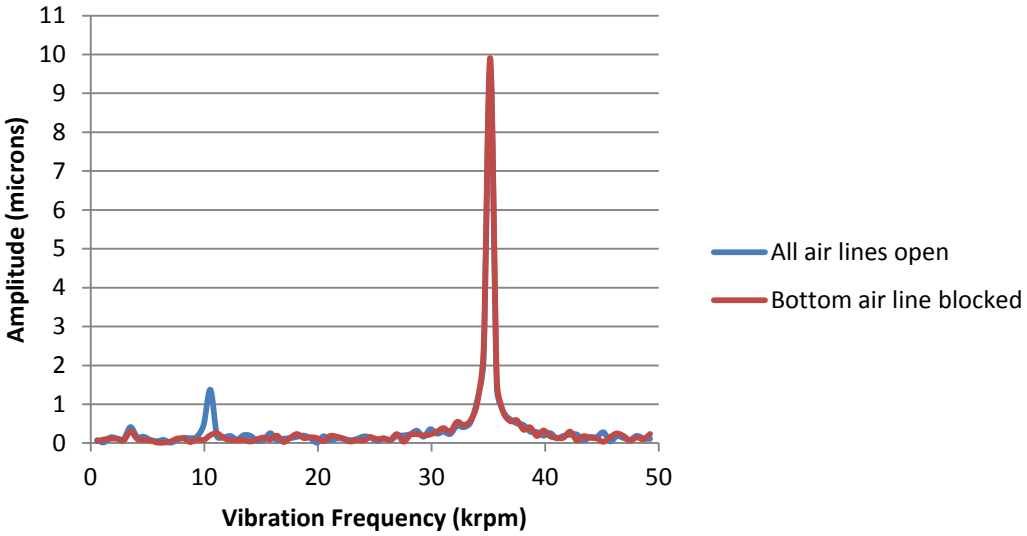
Amplitude (microns)
11
10
9
8
7
6
5
4
3
2
1
0
0
10
20
30
40
50
Vibration Frequency (krpm)
All air lines open
Bottom air line blocked

(A)

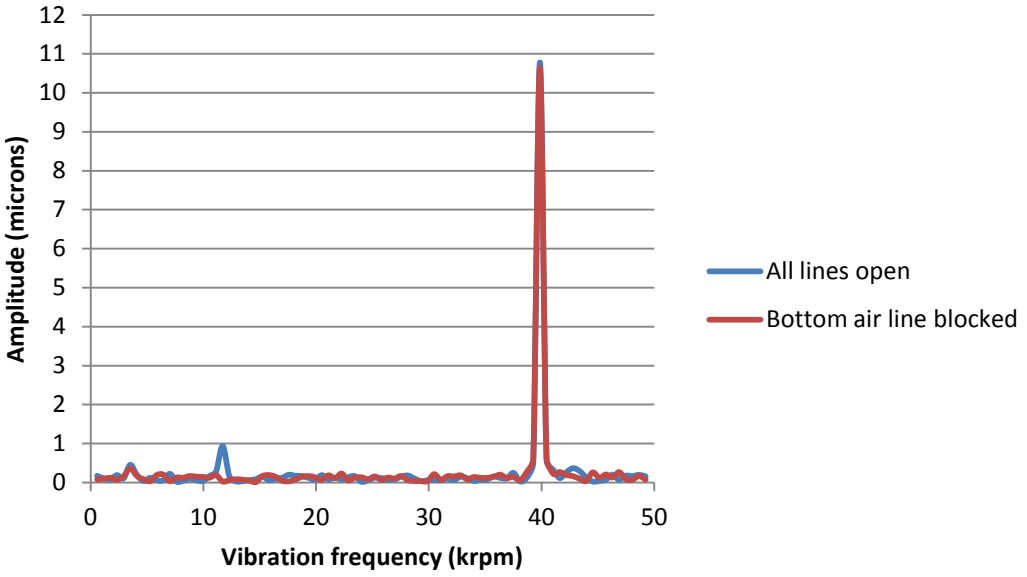
Amplitude (microns)
12
11
10
9
8
7
6
5
4
3
2
1
0
0
10
20
30
40
50
Vibration frequency (krpm)
All lines open
Bottom air line blocked

(B)

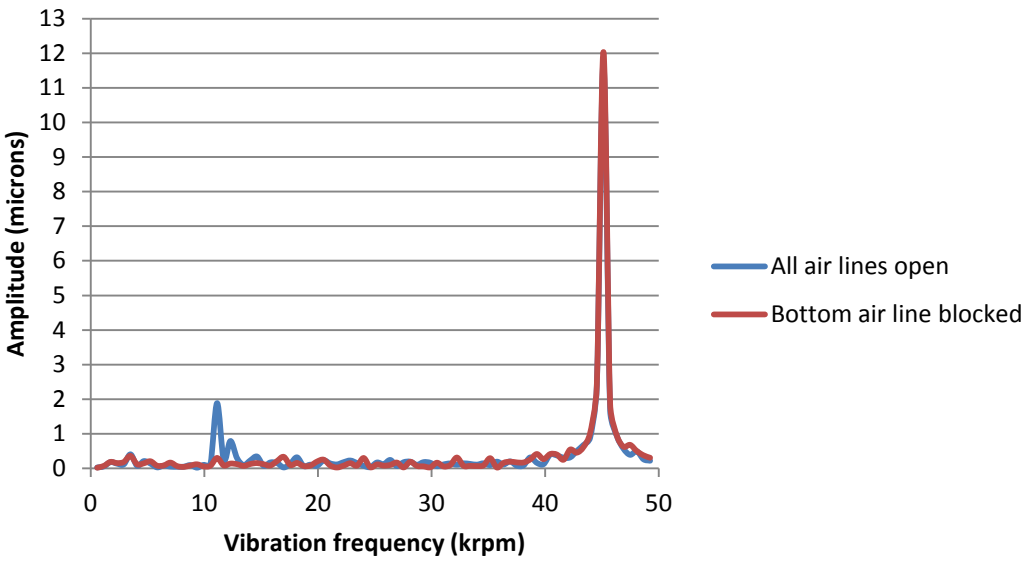

(C)

Figure 4-9 FFT Plots at 80 Psi (A) 35000 RPM (B) 40000 RPM (C) 45000 RPM

Chapter 5

Conclusion and Future Work

For HAFB, the small clearance makes eccentricity manipulation quite difficult. It is very challenging to increase HAFB eccentricity at low speeds, as the hydrodynamic pressure inside the bearing may not be high enough to support the load. For MIT microengine bearings, a large eccentricity may result in a physical separation of journal and bearing as low as 1 micron [19]. This suggests a deliberate choice of loading magnitude.

5.1 Conclusions from numerical studies

Numerical Simulations effectively support the idea of rotor stability with increased eccentricity for a three pad HAFB. In both tested cases, (60 Psi and 80 Psi) the onset of subsynchronous vibrations were delayed when tested with no bottom air injection line. For 60 Psi air feed pressure, the difference observed in the delay of instability is nearly 3000 RPM whereas for 80 Psi it is nearly twice at 7000 RPM.

Moreover, the orbit simulations suggest a higher bound range of speeds for the subsynchronous vibrations when the bottom air feed line was blocked. Though the onset of subsynchronous vibrations was nearly the same for both cases (all air lines open and bottom air line blocked) the amplitude rise of subsynchronous vibrations was quite rapid with all air lines open.

Higher rotor loading at 80 Psi proved to be more favorable than 60 Psi in delaying instability as mentioned earlier. Nevertheless, the speed range for which the subsynchronous vibrations were bound after blocking bottom air line was nearly the same for both cases (nearly 8000 RPM).

5.2 Conclusions from experimental studies

The simulation results over-predict the onset of subsynchronous vibrations. The simulations with both pressures (60 Psi and 80 Psi) anticipate the onset of subsynchronous vibrations around 33000 RPM. The initial experimental tests on the first two bearings failed to show any sign of subsynchronous vibrations before it was damaged (first at 39000 RPM and second at 48000 RPM) due to coating issues. Hence, the tests were performed on a subsequently developed bearing, which showed small amplitudes of subsynchronous vibrations at 35000 RPM.

The tests were conducted on a range of speeds (i.e. from 35000 RPM to 45000 RPM). The bearing was not tested for speeds beyond 45000 RPM to avoid any rotor damage resulting from thermal shaft growth and its centrifugal loading. Interestingly, when the bottom air lines were closed not much change was observed in the natural frequencies of the system but the amplitudes of subsynchronous vibrations diminished as expected.

5.3 Future Work

The main reason for the experimental tests not performed for higher amplitudes of subsynchronous vibrations was that it could damage the bearing. The shaft reflected large synchronous components at high speeds (due to coating issues). Hence, the shaft has to be coated with higher thickness to avoid failures [18] resulting from centrifugal loading and thermal growth at high speeds.

For the present study, subsynchronous amplitudes nearing 5 microns were effectively subdued by shaft loading. Experimental validation is needed to assess the effectiveness of shaft loading to subdue larger amplitudes of subsynchronous vibrations. In addition, the use of actuators to control air feed seems a plausible approach in the future for rotor stability.

Appendix A

Data Acquisition Using Lab View

A previously developed [16] LabVIEW VI is used for the data acquisition. Below is the front panel view of the VI showing FFTs, proximity signals and the journal's orbit.

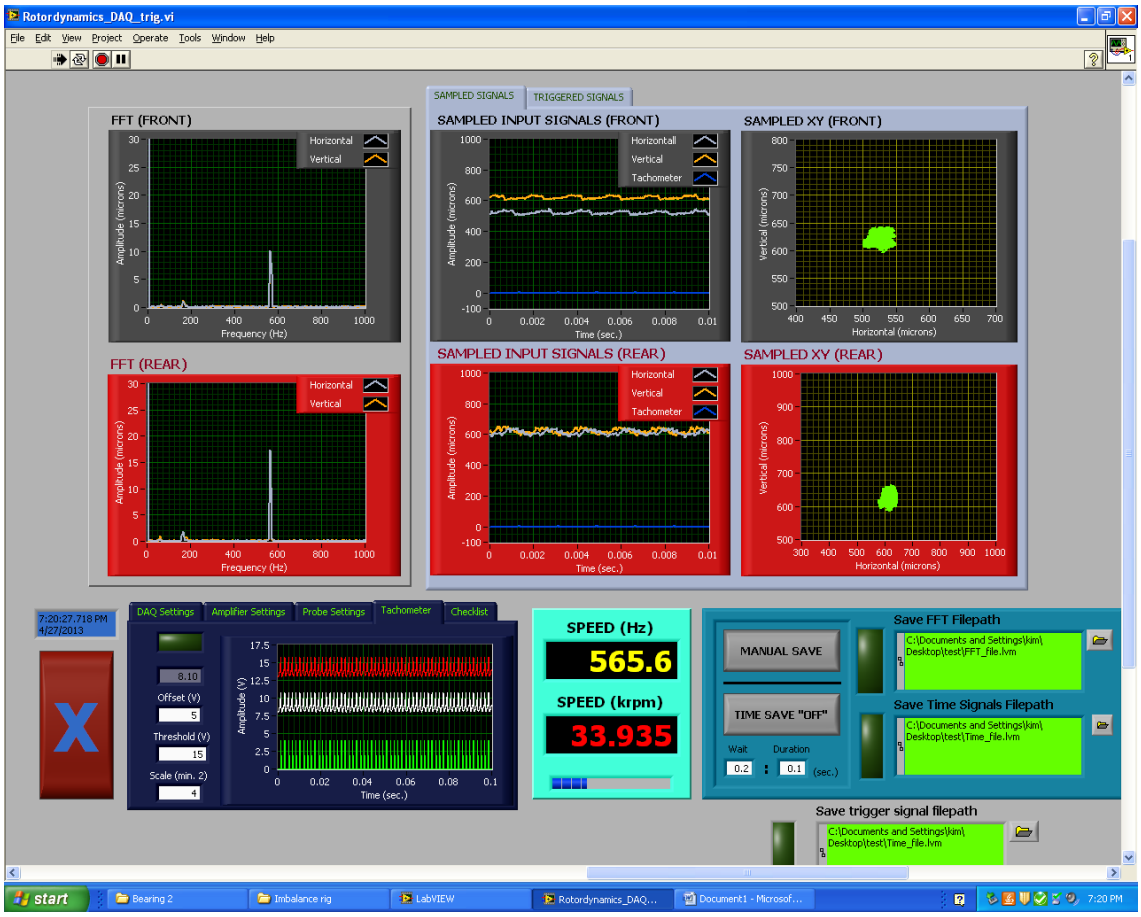

Figure A-0-1 LabVIEW VI Front Panel View

Appendix B

Shaft Failure

During the whole course of tests, the shaft was damaged twice. The first failure was beyond 39000 RPM with all air injection line operative at 60 Psi for both bearing. Due to the failure, the shaft comes to an instant halt resulting in extreme rubbing. The black rubbing mark on the shaft is the Teflon and the top foil (localized weld) that is welded to the surface of the shaft. The possibility of thermal runaway for the seizure is ignored because the system was under active cooling and the temperatures were monitored at different time intervals. It is also obvious in the waterfall plots that there were no signs of any instability. One possible explanation for failure could be shaft coating coming off at high speed, which then interfered with the bearing operation.

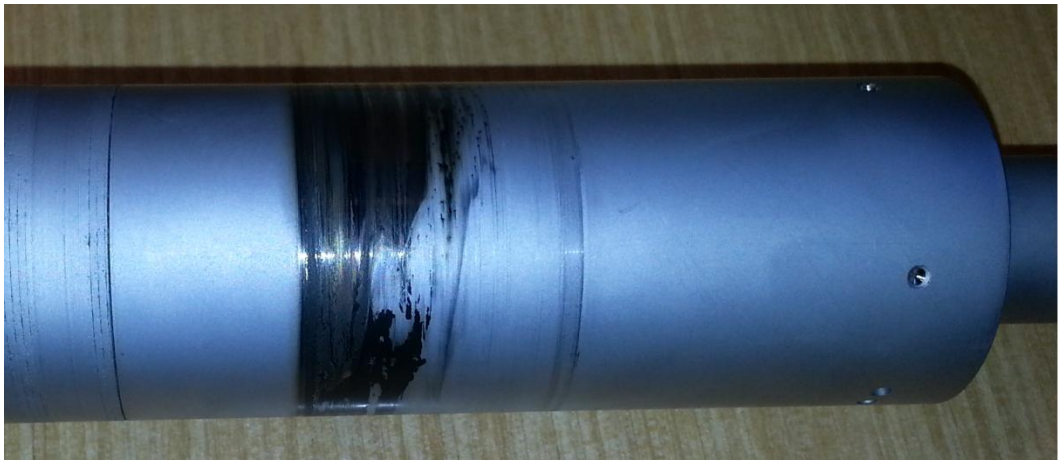

Figure B- 0-1 First Shaft Failure

In order to avoid coating related problems the new shaft was hard chrome coated to a depth of 0.01 in radially. The second shaft failure occurred beyond 48000 RPM with all air feed lines operative at 80 Psi. It is interesting to note that both shaft failures were

exactly at the same locations, it affirms that the shaft rather than the bearing is responsible for the failures. Again, no signs of subsynchronous vibrations or any other instability were witnessed at failure speed. The failure can be partially attributed to the shaft growth. The centrifugal loading of the shaft can significantly increase radial displacement due to shaft imbalance at a particular location and can cause local high spots (or bulging of coating) at high speeds. It is also necessary to include the effects of axial thermal gradient especially when the motor is also emanating heat to the shaft. Dykas and Howard [18] explained a similar shaft failure mechanism based on these the centrifugal growth and the axial temperature gradient.

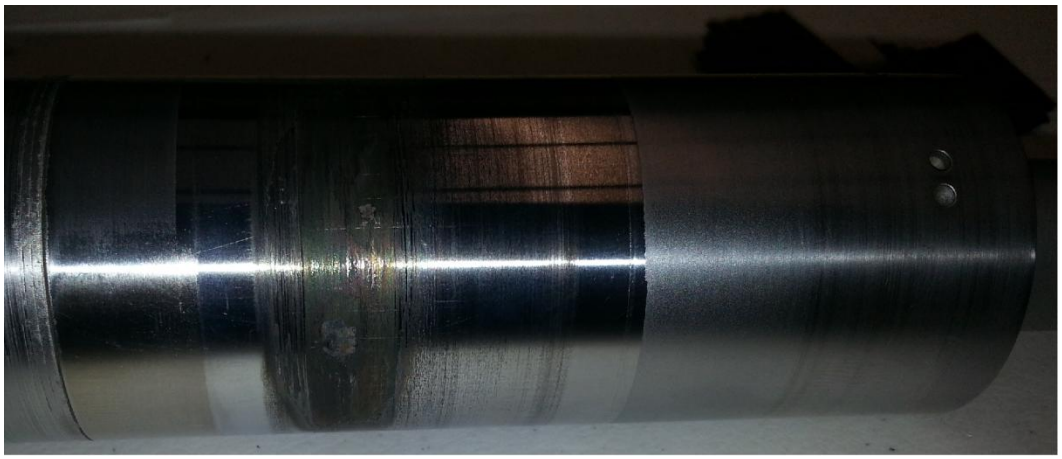

Figure B- 0-2 Second Shaft Failure

The failures resulted in extreme rubbing and complete damage of the bearing. The failures at such high speeds can be devastating but in the above-mentioned case, it was well restricted within the bearing sleeve. Shown below (Figure B- 0-3 Front Bearing failure) is a picture of the front bearing after second failure. Surprisingly, the rear bearing and the motor were intact and showed no signs of damage during both failures.

Figure B- 0-3 Front Bearing failure

Bibliography

[1] Kim, D., and Varrey, M., 2012, "Imbalance Response and Stability Characteristics of a Rotor Supported by Hybrid Air Foil Bearings," STLE Tribology Transactions**, 55**(4), pp. 529-538, DOI: 10.1080/10402004.2012.681341.

[2] Agrawal, G. L., 1997, "Foil Air/Gas Bearing Technology -- an Overview," International Gas Turbine & Aeroengine Congress & Exhibition, Orlando, FL, June 2-June 5,1997, ASME Paper No. 97-GT-347.

[3] San Andrés, L., 2010, "Modern Lubrication Theory," .

[4] Heshmat, H., 2006, "Evaluation of Coatings for a Large Hybrid Foil/MagneticBearing," ASME Paper no. IJTC2006-12328.

[5] Kim, D., and Park, S., 2006, "Hybrid Air Foil Bearing with External Pressurization," ASME Journal of Tribology, , pp. 63-69.

[6] Kumar, M., and Kim, D., 2008, "Parametric Studies on Dynamic Performance of Hybrid Air Foil Bearings," Journal of Engineering for Gas Turbines and Power**, 130**(6), pp. 062501-1-062501-7.

[7] Kim, D., 2012, *Foil bearings with multiple pads with controlled assembly clearance*, Disclosed to Office of Intellectual Property, University of Texas at Arlington.

[8] Lee, D., and Kim, D., 2011, "Three-Dimensional Thermo-Hydrodynamic Analyses of Rayleigh Step Air Foil Thrust Bearing with Radially Arranged Bump Foils," STLE Tribology Transaction**, 54**(3), pp. 432-448.

[9] Dykas, B., Bruckner, R., DellaCorte, C., Edmonds, B., and Prahl, J., 2008, "Design, Fabrication, and Performance of Foil Gas Thrust Bearings for Microturbomachinery Applications," ASME Turbo Expo 2008, Berlin, Germany, June 9-13, ASME Paper number GT2008-50377.

[10] SanAndrés, L., Rubio, D., and Kim, T. H., 2007, "Rotordynamic Performance of a Rotor Supported on Bump Type Foil Gas Bearings: Experiments and Predictions," Journal of Engineering for Gas Turbines and Power**, 129**, pp. 850-857.

[11] Wilde, D., and SanAndrés, L., 2003, "Comparison of Rotordynamic Analysis Predictions with the Test Response of Simple Gas Hybrid Bearings for Oil-Free Turbomachinery," , ASME Paper GT-2003-38859.

[12] Osborne, D. A., and San Andrés, L., 2006, "Experimental Response of Simple Gas Hybrid Bearings for Oil-Free Turbomachinery," Journal of Engineering for Gas Turbines and Power**, 128**, pp. 626-633.

[13] Zhu, X., and San Andrés, L., 2004, "Rotordynamic Performance of Flexure Pivot Hydrostatic Gas Bearings for Oil-Free Turbomachinery," ASME Turbo Expo 2004, Vienna, Austria, ASME Paper No. GT2004-53621.

[14] Kim, D., 2011, "Tribology Notes," .

[15] Kim, D., 2007, "Parametric Studies on Static and Dynamic Performance of Air Foil Bearings with Different Top Foil Geometries and Bump Stiffness Distributions," ASME Journal of Tribology**, 129**(2), pp. 354-364.

[16] Rimpel, A.M., 2008, *ANALYSIS OF FLEXURE PIVOT TILTING PAD GAS BEARINGS WITH DIFFERENT DAMPER CONFIGURATIONS*, Texas A&M University.

[17] P. Shetty, 2010, *IMBALANCE RESPONSE OF A FOUR DEGREE OF FREEDOM RIGID ROTOR SUPPORTED BY HYBRID THREE PAD AIR FOIL BEARING,* MS thesis, UTA.

[18] Dykas, B., and Howard, S. A., 2004, "Journal Design Considerations for Turbomachine Shafts Supported on Foil Air Bearings," STLE Tribology Transactions**, 47**(3), pp. 508-516.

[19] E. Piekos, 2000, *Numerical Simulation of Gas-Lubricated Journal Bearings for Microfabricated Machines,* PHD thesis, MIT.

Biographical Information

Sandesh Gudemane graduated with Bachelors in Mechanical Engineering from Visvesvaraya Technological University, India in May 2008. He worked for 2 years as a Mechanical Engineer undertaking several challenging projects. Later, he decided to pursue masters in mechanical engineering and joined Microturbomachinery and Energy System Lab at University of Texas at Arlington. While working on his masters he also gained some intern experience at SouthernVac LLC. In the future, he intends to work in the energy sector.